Development of Non-Spherical Platinum Catalyst with Functionalized Carbon Supports for Proton Exchange Membrane Fuel Cells

by

Mark Lim

A thesis

presented to the University of Waterloo

in fulfillment of the

thesis requirement for the degree of

Master of Applied Science

in

Mechanical and Mechatronics Engineering

Waterloo, Ontario, Canada, 2023

© Mark Lim 2023

Author's Declaration

I hereby declare that I am the sole author of this thesis. This is a true copy of the thesis, including any required final revisions, as accepted by my examiners.

I understand that my thesis may be made electronically available to the public.

Abstract

Energy conversion devices capable of zero-emission operation are needed to limit the impacts of anthropogenic climate change. Proton exchange membrane (PEM) fuel cells are well suited to address this need, as they can produce electricity directly from the chemical energy stored within green hydrogen and oxygen, emitting only water and heat. A major component of their cost is platinum (Pt) based catalyst, which is needed to catalyze the oxygen reduction reaction (ORR). Therefore, the performance and durability of Pt-based catalysts must be improved to drive down the cost of PEM fuel cells. One strategy is to adopt non-spherical morphologies, which can increase the active surface area and inherent ORR activity compared to spherical Pt nanoparticles (NPs). Another strategy is to disperse the NPs on an optimally designed carbon support, forming a platinum/carbon (Pt/C) catalyst. The carbon support can be functionalized to introduce binding sites and promote dispersion of Pt NPs. While research has proven both these strategies effective, their benefits can only be fully realized if the Pt/C catalyst is synthesized in a facile and scalable manner while retaining its catalytic properties. As such, synthesis methods that use a one-pot approach and avoid difficult-to-remove surfactants are advantageous. In addition, practical applications necessitate the catalyst to perform well not only electrochemically, but also in full-cell tests. To date, few studies have emphasized the importance of facile/scalable synthesis and full-cell performance for shape-controlled Pt catalysts and functionalized carbon supports.

In this study, a surfactant-free one-pot method is developed to synthesize non-spherical Pt NPs on Ketjen Black carbon, and the catalysts are characterized using physical and electrochemical methods. First, the catalyst is synthesized in small batches on three varieties of Ketjen Black: non-functionalized (Pt/KB), oxidation-treated (Pt/KB-O), and

nitrogen-doped (Pt/KB-N). Then, the catalysts are synthesized on a 10x larger scale to evaluate the impact of scaling up the synthesis. Surface area measurement and X-ray photoelectron spectroscopy measurements are done on the functionalized carbons, while transmission electron microscope imaging, X-ray diffraction, and thermogravimetric analysis are used to characterize the Pt/C catalysts. Electrochemical characterization on a rotating disk electrode setup is done to measure the catalysts' ORR activity. Accelerated stress tests are run by cycling the potential between 0.5-1 V and 1-1.5 V to evaluate their durability against catalyst degradation and carbon corrosion, respectively.

Physical tests confirm that both oxidation treatment and nitrogen doping affect the carbon surface chemistry and microstructure, which in turn affect the properties of the supported Pt catalysts. For both Pt/KB-O and Pt/KB-N, the functional groups on the carbon serve as binding sites, preventing the NPs from agglomerating. However, the carbon affects the NP size distribution, with Pt/KB-O containing larger NPs compared to Pt/KB and Pt/KB-N. When the synthesis is scaled up, Pt/KB changes greatly with its small NPs being replaced by nanowires or nanorods, whereas Pt/KB-O and Pt/KB-N remain visually similar between their small- and large-scale versions. Therefore, functional groups on the carbon foster a more predictable or scalable catalyst morphology when using this one-pot synthesis method.

Electrochemical tests reveal both similarities and differences between the catalysts on different carbon supports. Pt/KB-O achieves only similar or slightly lower ORR activity as Pt/KB, possibly because of poisoning from the sulfonate-based ionomer used in the test, and Pt/KB-N achieves similar or slightly higher ORR activity. All the catalysts are similarly durable when cycled between 0.5-1 V, showing that carbon functionalization does little to prevent Ostwald ripening. However, Pt/KB-O is the most durable when

cycled between 1-1.5 V, showing that oxygen functional groups change the susceptibility to carbon corrosion or NP detachment. Unexpectedly, all three catalysts achieve higher ORR activity when the synthesis is scaled up, attributed to the high surface area and activity of Pt nanorods. These results will help inform the implementation of shape-controlled Pt catalysts and functionalized carbon supports in large scale.

Acknowledgements

First of all, I would like to acknowledge all the professors who have guided this thesis work. I am grateful to Dr. Xianguo Li, who not only provided me with valuable advice, but was always willing to discuss matters pertaining to both this thesis work and my Master of Applied Science degree in general. I also thank Dr. Samaneh Shahgaldi, who provided additional guidance for my work and expressed clear support of this project. In addition, I thank Dr. Xiaoyu Wu and Dr. Yimin Wu for their willingness to review my thesis as committee members. The contributions of all these individuals have not only refined my thesis work, but also ensured this project would become a highly valuable and rewarding educational experience for me.

Much of the experimental work would not have been possible without the help of individuals from within my research group, elsewhere in the University of Waterloo, and beyond. I would like to acknowledge the staff at the Waterloo Advanced Technology Laboratory (WATLab), who helped with the TEM and XPS measurements, and the staff at the Chemical Engineering Analytical Lab, who assisted the TGA, BET area, and XRD measurements. I also appreciate the work from Mohmmad Khalid, who prepared the nitrogen-doped carbon material and helped me interpret electrochemical data. Furthermore, I thank Shawn Tan for introducing me to our research group's catalyst synthesis and RDE test procedures, upon which this thesis work is based.

Lastly, I could not forget to acknowledge my parents, whose support has enabled me to flourish in my studies up to and including this Master of Applied Science degree.

Table of Contents

List of Figures

List of Tables

Abbreviations

AST accelerated stress test 48, 49, 70, 73, 77, 80, 81

BET Brunauer-Emmett-Teller 32, 42, 43, 50, 53, 63, 67, 68, 76, 79, 80

CL catalyst layer 4, 6, 8, 10, 17–19, 22, 28, 31, 35, 36, 81

CNT carbon nanotube 18–20, 31, 76

CV cyclic voltammetry 33, 46–48, 62, 64, 65, 70, 73

DIW deionized water 39–42, 46

DMF N,N-dimethylformamide 25, 26, 36, 41, 55, 58, 81, 82, 106

DOE United States Department of Energy 3, 7, 31, 48, 49

ECSA electrochemically active surface area 7, 8, 11, 13, 19, 20, 33, 36, 46–48, 54, 64, 65, 67, 68, 70, 73, 77, 80

EG ethylene glycol 24–26, 36, 41, 55, 58, 81, 82, 106

GDL gas diffusion layer 4, 6, 28, 34

Chapter 1

Introduction

1.1 Motivation

Climate change has driven an urgent need for energy conversion technologies that are free of harmful pollutants and compatible with renewable energy sources. According to the International Energy Agency, global energy consumption, electricity demand, and CO_2 emissions have all been trending upwards during the last few decades [1]. These trends will increasingly harm the environment and exacerbate climate change unless mitigation actions are taken promptly. One such action is a large-scale shift from carbon-emitting to renewable energy sources. In 2020, global usage of renewable energy increased even as the demand for CO_2-emitting fossil fuels such as oil, coal, and natural gas experienced a decline [1]. Therefore, as renewable energy sources undergo rapid adoption, clean energy conversion technologies suited for a sustainable energy infrastructure must be developed to utilize these sources.

A technology compatible with renewable and carbon-neutral energy sources is the fuel cell, a power-generation device designed to convert chemical energy directly into electrical energy. While some types of fuel cells are designed to use carbon-containing fuels, the majority can operate with hydrogen (H_2) and oxygen (O_2), thus classifying them as zero-emission conversion devices. Fuel cells operating on green H_2 can play an important role in decarbonizing the global energy system, with H_2 anticipated to contribute up to 18-24% of final energy demand by the middle of this century [2, 3]. Fuel cells merge characteristics of both batteries and heat engines: they are conceptually similar to batteries as both are electrochemical devices containing electrodes and electrolytes, but they are architecturally more similar to heat engines as both are open systems with the reactants stored externally [4]. Compared to heat engines, fuel cells enable high energy conversion efficiency, low pollutant emissions, fast transient load response, quiet operation, low maintenance requirements, and modular design [4].

Proton exchange membrane (PEM) fuel cells are one of the most well-developed and promising types of fuel cells, and they are suitable for applications in transportation and portable power, sectors that are most difficult to decarbonize with conventional energy conversion technologies. Anticipated as a major component of the hydrogen-based energy economy, PEM fuel cells are recognized as emerging clean power and propulsion systems for markets in sustainable aviation [5], passenger vehicles, and heavy-duty transportation [6, 7, 8]. Compared to batteries, PEM fuel cells feature lower power density but higher energy density, and fuel cells work well with centralized H_2 refueling infrastructure, making them ideally suited to complement batteries in electric vehicles [7]. Research and industrial efforts directed towards commercializing PEM fuel cells have grown because they can partially replace the role of internal combustion engines in an environmentally friendly manner.

Despite tremendous progress in the last few decades, PEM fuel cell systems remain expensive for widespread adoption as energy conversion devices. According to the United States Department of Energy (DOE), next-generation PEM fuel cell technology is approaching technical targets (efficiency, durability, and mass production cost) for 2025, but commercially available units remain far too expensive [9]. A substantial portion of the cost is platinum (Pt) based catalyst, which is estimated to comprise over 40% of the total cost of a PEM fuel cell [10]. The total platinum group metal content in a typical automotive fuel cell stack greatly exceeds that of the catalytic converter in a conventional internal combustion engine vehicle [7, 11]. Furthermore, as production expands in the future, the cost of other components will decrease because of economies of scale, but the cost of Pt could remain high, so the relative contribution of Pt to total cost may increase [6]. Therefore, the Pt loading must be reduced to make PEM fuel cells more economical. This reduction in Pt loading is accomplished by improving the activity/durability of the catalyst and optimizing the fuel cell electrodes to maximize catalyst utilization.

1.2 Fuel Cell Working Principle and Components

An acid-electrolyte fuel cell operating on hydrogen and oxygen facilitates two electrochemical half-cell reactions. On the anode, the hydrogen oxidation reaction (HOR) splits hydrogen molecules into protons and electrons:

$$H_2 \rightarrow 2H^+ + 2e^- \tag{1.1}$$

The resulting protons migrate through a proton-conducting electrolyte from anode to cath-

ode, and the electrons travel through a separate circuit. Electrical power is harvested from the electrons flowing through this external circuit. On the cathode, the protons, electrons, and oxygen molecules combine into water as described by the oxygen reduction reaction (ORR):

$$2\text{H}^+ + 2\text{e}^- + \frac{1}{2}\text{O}_2 \rightarrow \text{H}_2\text{O} \tag{1.2}$$

Summing the HOR and ORR yields the following global reaction [4]:

$$\text{H}_2 + \frac{1}{2}\text{O}_2 \rightarrow \text{H}_2\text{O} + \text{electrical energy} + \text{waste heat} \tag{1.3}$$

Figure 1.1 illustrates the functions of a membrane-electrode assembly (MEA), which is the core component of a PEM fuel cell enabling the conversion of chemical energy into electrical energy. The MEA consists of a PEM separating two electrodes. Each electrode contains a nano-porous catalyst layer (CL) and macro-porous gas diffusion layer (GDL). In addition to these two components, a microporous layer can be coated onto the GDL surface facing the CL [12]. The GDLs distribute reactant gases into the CL and facilitate product water removal from the fuel cell. The CL microstructures contain reaction sites to catalyze the HOR and ORR at the anode and cathode, respectively, while facilitating transport of protons, electrons, reactants, and products. In between the electrodes, the PEM enables proton transport from anode to cathode while being impervious to gases and electrons, thus preventing H_2 and O_2 from combining directly.
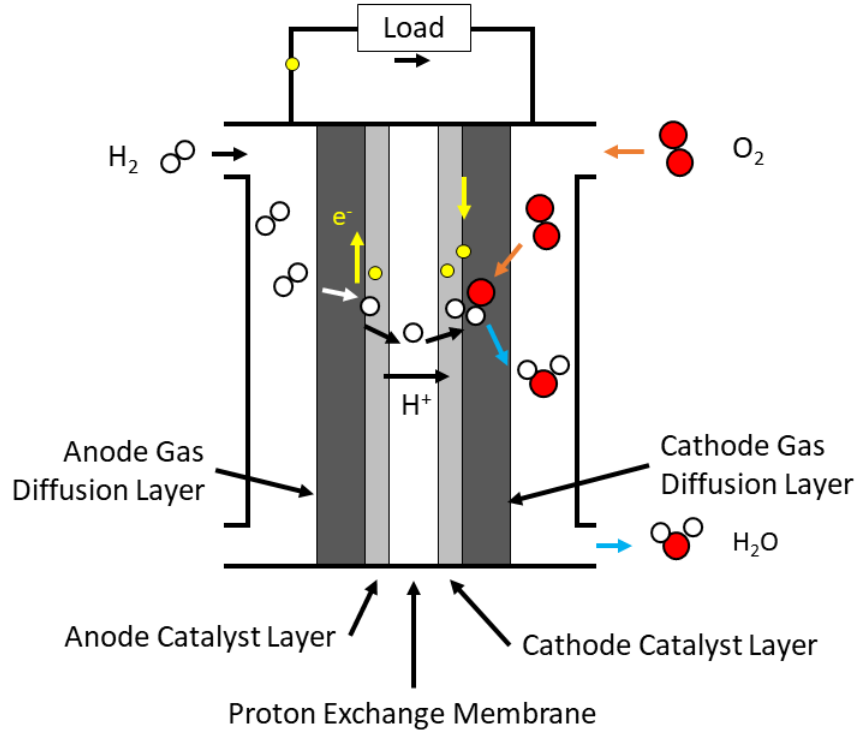
Figure 1.1: Operating principle of the PEM fuel cell

The voltage output of a fuel cell is the difference between the reversible voltage, E_r, and the sum of irreversible losses known as overpotentials. At a temperature of 25°C and pressure of 1 atm, and assuming the product water is liquid, the reversible voltage is 1.229 V. The main sources of overpotential arise from reaction kinetics, ion and electron transport, and mass transport:

$$E = E_r \left(\text{at } T, p \right) - \eta_{act} - \eta_{ohm} - \eta_{conc} \tag{1.4}$$

where E is actual cell voltage and η_{act}, η_{ohm}, and η_{conc} are called activation, ohmic, and concentration overpotential, respectively. Activation overpotential is attributed to the electrode's inherent kinetics, which is quantified by the exchange current density. This overpotential is minimized by aiming for a high exchange current density, which is dictated by the catalyst material and electrode design [4, 13]. Ohmic overpotential includes both protonic (ionic) and electronic resistance, characterized by a linear voltage-current relationship as per Ohm's Law. In a PEM fuel cell, multiple components including the PEM, CL, and GDL contribute to the total ohmic resistance. Concentration overpotential traditionally describes molecular diffusion of gaseous H_2 and O_2 from bulk phase to the reaction sites; therefore, it depends on the CL, GDL, and reactant supply channels. However, recent studies suggest that the effects of Knudsen diffusion and local O_2 transport in the cathode CL are also important [14, 15]. Therefore, fuel cell catalysts and CLs must be optimized because they affect all of the overpotentials in Equation 1.4.

1.3   PEM Fuel Cell Catalysts and Catalyst Supports

In low-temperature fuel cells such as PEM fuel cells, a catalyst is required to accelerate the HOR/ORR kinetics and generate practical amounts of power. Electrocatalysis allows the reaction to proceed more quickly by facilitating reactant adsorption on a catalyst surface, transformation of the reactants into desired products, and desorption of the products [4]. For low-temperature hydrogen fuel cells, electrocatalysis is most important for the ORR because the kinetics of the ORR can be several orders of magnitude slower compared to the HOR [4]. According to theoretical studies, the ORR performance of different catalyst materials is related to *O and *OH adsorption energies on their surfaces [16]. Platinum

6

(Pt) has been determined to be the best single-element ORR catalyst owing to its nearly-optimal binding energy [17], so it is the most commonly used catalyst in PEM fuel cells.

The activity of an electrocatalyst is evaluated using three quantities: electrochemically active surface area (ECSA), specific activity (SA), and mass activity (MA). ECSA is defined as the active catalyst surface area per unit mass of Pt (cm^2_{Pt}/mg_{Pt}), SA as current per unit area (A/cm^2_{Pt}), and MA as current per unit mass (A/mg_{Pt}) [6]. These quantities are related as follows:

$$MA = ECSA \times SA \tag{1.5}$$

Clearly, increasing ECSA or SA results in higher MA, thereby decreasing the amount of Pt required for a fuel cell to achieve a given level of performance. The widely cited target for light-duty transportation PEM fuel cells, set by the DOE for year 2020, is 0.44 A/mg_{Pt} [18]. In addition to its beginning-of-life MA, the catalyst must maintain an adequate MA throughout the fuel cell's operating lifetime to satisfy system durability requirements.

As shown by Equation 1.5, the MA of a fuel cell catalyst depends not only on its intrinsic catalytic activity (i.e., SA) but also the surface area available for heterogeneous catalysis (i.e., ECSA). Therefore, both the elemental composition and morphology must be considered when developing novel nanomaterials for electrocatalytic applications. State-of-the-art PEM fuel cells typically use nanometer-sized Pt particles as the catalyst because of their high area-to-volume ratio, a critically important feature for heterogeneous catalysis. However, the quasi-spherical morphology of commercially available Pt nanoparticle (NP) catalysts is suboptimal because their area-to-volume ratio and intrinsic activity are still lower than those of non-spherical structures [16, 19]. Therefore, if non-spherical nanos-

tructures can be developed instead, they would potentially increase the catalyst's ECSA, SA, and MA, and consequently the utilization of Pt in low-temperature fuel cells.

Shape control is a promising approach for metal nanocatalysts because not only does it inherently increase the active surface area and catalytic activity, but it can be combined with other strategies to improve upon commercially available electrocatalysts. Shape-controlled nanostructures increase the area-to-volume ratio compared to spherical or quasi-spherical NPs, thus increasing the catalytically active area. In addition, by realizing specific crystal facets (e.g., (100), (111), (110)) on the nanoscale, shape control alters the catalyst's chemical and electronic interactions, leading to controllable catalytic selectivity and improved performance [20]. This concept can also be combined with alloy designs to create highly active electrocatalysts. Alloying modifies the catalyst's surface electronic structure via ligand and strain effects [16], helping optimize the adsorption energy of oxygen species and increasing catalytic activity. Examples of elements that can be alloyed with Pt include transition metals (e.g., Ni, Fe, Co) and rare earth metals (e.g., Ce, La, Y) [21]. One particular design that has garnered much attention for ORR catalysis is Pt-Ni nanocrystals dominated by (111) surfaces [19].

To further improve its dispersion, stability, and electronic conductivity, as well as forming sufficiently large pore structures for reactant mass transport, Pt catalyst is often deposited on a much larger carbon substrate, creating a carbon-supported Pt catalyst (Pt/C). The catalyst support is a crucial component of the CL and can impact the overall performance of a PEM fuel cell. Carbon is a reasonable and widely used support for Pt-based catalysts in fuel cells, owing to its natural abundance and favorable properties (e.g., electrical conductivity). Similar to the catalyst itself, specific design strategies can be applied to improve the properties of the carbon support. One such strategy is to choose an optimal

geometry. Various carbon materials, ranging from carbon blacks to graphitized materials, can be used as the support [7]. Experimental studies show that the choice of carbon support impacts both the activity and durability of the catalyst [22, 23]. Another strategy is to functionalize the carbon using methods such as oxidizing acid treatment [24] and nitrogen doping [7] to introduce surface groups that serve as nucleation sites for Pt NPs. Doing this especially benefits certain kinds of carbon materials, such as carbon nanotubes. In addition to tuning the performance of Pt catalysts, functionalized carbons can serve as metal-free catalysts by themselves [25], so they are of great interest for energy applications in general.

1.4 Challenges of Adopting Shape-Controlled Platinum Catalysts

A major challenge to using newly designed catalysts in commercially viable PEM fuel cells is synthesizing such catalysts on a scale suitable for mass production. Practical and scalable synthesis of high-activity Pt-based catalysts remains a poorly addressed topic in current literature. Experimental studies that center on catalyst development typically synthesize the catalysts in small batches, which may be convenient for lab-scale testing and design down-selection [26]. However, such procedures must be scaled up to be adopted into large-scale production. It remains challenging to synthesize shaped NP catalysts while maintaining control of their performance-enhancing physicochemical properties [27]. Because of this challenge, shape-controlled Pt/C is often synthesized using a multi-step method to maximize control of the reaction conditions. However, multi-step methods are inherently complex, and they may fail to produce stable and well-dispersed Pt NPs

on the carbon support. Consequently, mass production of Pt/C catalysts would benefit from adopting the so-called one-pot synthesis method [28]. Developing scalable one-pot synthesis methods is an important part of adopting advanced Pt-based catalysts in large scale.

Furthermore, shape-controlled Pt-based catalysts that theoretically have high electrochemical activity do not necessarily show high performance when integrated into the CL of an MEA [26, 29]. Many recent review articles acknowledge the relationship between CL design and catalyst performance as an emerging research topic for PEM fuel cells [6, 19, 30]. The performance gap exists because half-cell tests are typically performed on very thin CLs immersed in liquid electrolyte solutions, whereas MEA electrodes must facilitate the simultaneous transport of gaseous reactants, product water, and ions. As shown in Figure 1.2, a typical CL is composed of solid Pt/C, proton-conducting ionomer, and gas pores, and a zone containing all three of these phases is known as a three-phase boundary (TPB). The ionomer coats the Pt/C catalyst as a thin film, and its primary functions are to bind the catalyst and conduct H^+ between the PEM and catalyst active sites. This film should ideally have uniform thickness to minimize O_2 and H^+ transport resistances [31]. Therefore, any properties of the Pt/C catalyst that may affect the ionomer layer or overall mass/ion transport properties can potentially affect MEA performance. One such example is functionalizing the carbon with nitrogen doping, which may foster a more uniform ionomer film and minimize O_2 transport resistance at the catalyst interface [32]. The impacts of catalyst and support material on MEA performance must be considered to realize the full potential of high-activity catalysts in fuel cell applications.
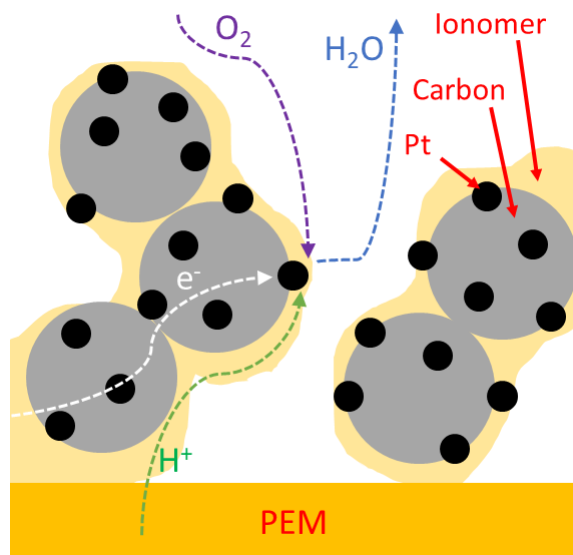
Figure 1.2: Conventional cathode CL structure

1.5 Objectives and Outline of Thesis

The objectives of this thesis work are to:

1. Synthesize shape-controlled and carbon-supported Pt catalysts in one step, using what is often referred to as one-pot synthesis

2. Evaluate the effects of carbon support functionalization on the non-spherical Pt catalyst, followed by a comparison of its performance when synthesized in both small and large batches

This thesis work centers on non-spherical Pt NP catalysts supported on functionalized carbon materials. The developed catalysts are characterized physically and electrochemically for their performance and stability. Rather than simply aiming for the highest ECSA

and SA based on electrochemical tests, the catalyst is developed in a manner suitable for mass production and application in MEAs. The selected catalyst synthesis method is a one-pot and surfactant-free solvothermal method that has previously been used to produce various non-spherical Pt nanostructure catalysts. To address gaps in current literature, this study directly compares two carbon functionalization methods (oxidizing acid treatment and nitrogen doping) in terms of how they affect shape-controlled Pt catalysts, and also scales up the catalyst synthesis to progress the application of shape-controlled Pt catalysts in practical PEM fuel cells.

The contents of this thesis are organized as follows. Chapter 1, the current chapter, introduces the principles of the PEM fuel cell and its electrodes to set the context for this thesis work. Chapter 2 summarizes recent literature concerning shape-controlled Pt-based catalysts, carbon support materials and functionalization methods, Pt and Pt/C catalyst synthesis, fuel cell performance of shape-controlled catalysts, and experimental methods for evaluating the catalysts. The chapter concludes by reiterating the contributions of this thesis in the context of current literature. Chapter 3 details all the experimental methods used to synthesize and characterize the Pt/C catalysts in this work. Chapter 4 presents the results of these experiments and discusses their significance as per the two objectives listed above. Lastly, Chapter 5 summarizes the key results from this work and suggests directions for future work.

Chapter 2

Literature Review

2.1 Shape-Controlled Platinum Nanostructure Catalysts

Shape-controlled Pt and Pt-alloy nanocrystals have garnered attention as potential PEM fuel cell catalysts because of their high MA compared to commercially available pseudo-spherical Pt NPs. The thermodynamically stable NP shape for an fcc metal such as Pt is a type of truncated octahedron [33], which is dominated by low-index facets ((100) and (111)) but features a lower surface-area-to-volume ratio compared to most morphologies such as cubes and octahedra. This is undesirable because high surface area is important for heterogeneous catalysis. Therefore, most non-spherical morphologies have potential to increase the catalyst's ECSA. In addition to this effect, shape control exposes specific crystal facets and creates defect sites (e.g., edges, corners), whose electronic structures dictate the adsorption energies of reactant species on the Pt surface [34]. This adsorption

13

strength can be tuned to maximize SA. To realize the benefits of specific facets in the nanoscale, Pt-based catalysts can be synthesized as polyhedral nanocrystals such as cubes, octahedra, cuboctahedra, and truncated octahedra, among other geometries [19].

Cubic Pt-based NPs have received attention as an advanced electrocatalyst design because of the properties of the Pt(100) surface. Relative to Pt(111), the Pt(100) facet demonstrates superior activity in a variety of reactions including the ORR in H_2SO_4 electrolyte, ammonia oxidation in NaOH electrolyte, benzene hydrogenation, and NO reduction [35]; however, it is less stable at high potentials in H_2SO_4 electrolyte [36]. Several studies have explored the potential of Pt nanocubes as fuel cell catalysts. For example, carbon-supported Pt nanocubes have been synthesized in a facile manner by optimizing the heat treatment temperature and duration. This class of catalyst achieves better formic acid oxidation performance than commercial Pt/C owing to improved catalyst utilization [37]. Another study, which aimed to eliminate expensive and difficult-to-handle chemicals in the synthesis process, produced 9 nm sized nanocubes that demonstrate enhanced catalytic activity and good durability [35]. In addition to improved ORR activity, Pt nanocubes exhibit good CO oxidation performance. CO is known to poison the Pt catalyst surface and deteriorate fuel cell performance [38], so preferential oxidation of CO into CO_2 is useful for PEM fuel cells fueled impure H_2 or carbon-containing fuels such as methanol and ethanol. CO stripping and fuel cell tests show that CO oxidizes at lower potentials on (100)-oriented Pt NPs compared to polycrystalline Pt/C, and using Pt nanocubes as the anode catalyst increases fuel cell performance (after normalizing for Pt surface area) [39].

Another facet that offers enhanced catalyst performance is the Pt(111) surface. Octahedral and tetrahedral NPs are comprised solely of (111) surfaces, whereas cuboctahedral, truncated octahedral, and hexagonal NPs combine (111) with (100) surfaces. Compared

14

to other crystal planes, Pt(111) features dense atomic packing and cohesive energy, leading to high catalytic efficiency and surface stability [40]. Tetrahedra and octahedra theoretically exhibit the highest ORR activity amongst low-index faceted Pt nanocrystals, including cubes and truncated octahedra [41]. However, in practice, sulfonate groups from the ionomer/electrolyte tend to adsorb more strongly onto the Pt(111) surface compared to Pt(100) and Pt(110) [41, 42], thus hindering the ORR activity of shapes that contain only Pt(111). As a result, shapes that combine Pt(100) and Pt(111) could possibly be better for ORR catalysis, with hexagonal Pt NPs having reported higher activity than tetrahedral, octahedral, cubic, and spherical NPs [43]. However, efforts are underway to mitigate sulfonate poisoning from the ionomer [44, 45], so the detrimental effect of sulfonate adsorption on Pt(111) could be reduced in this manner.

Pt NPs with preferential (111) facets are often implemented as alloys with other metals, thus combining the catalytic benefits of alloying and shape control. This strategy aims to tune the binding energies of reaction intermediates. The optimum ORR activity correlates to binding energies slightly weaker than those of Pt(111) [19] and thus requires alloying to achieve. For example, a study demonstrated that the $Pt_3Ni(111)$ surface increases the SA (measured at 0.9 V) tenfold compared to Pt(111) as a result of reduced OH adsorption, which leads to more available active sites for O_2 [46]. The exceptional activity of $Pt_3Ni(111)$ has motivated researchers to create octahedral Pt-Ni NP catalysts, which can achieve good performance in practical PEM fuel cell electrodes [47]. Similar to Pt nanocubes, octahedral Pt_3Ni catalysts show good CO oxidation activity and selectivity in temperatures of up to approximately 100°C [48]. Another example of a Pt-alloy catalyst dominated by (111) surfaces is the Pt-Pd tetrahedron, which has been proposed as an electrocatalyst for direct alcohol fuel cells. This design can be optimized to improve methanol and ethanol oxidation and reduce adsorption of poisoning species [49].

Other advanced Pt-based catalyst designs that have been explored include high-index faceted NPs and hollow nanoframes. NPs with high-index facets can yield high catalytic activity because their many surface defects (e.g., steps, edges, kinks) serve as highly active sites, although they are prone to degradation [16] and generally difficult to synthesize. One example of such a design is the Pt-Pd concave nanocube, which can be synthesized by controlling the nucleation and growth process such that Pt atoms pile up on the edges and vertices of nanocubes, forming Pt-rich high-index facets. This design demonstrates improved MA and SA over commercial Pt/C and ordinary Pt-Pd nanocubes [50]. Solid polyhedral NPs can also transform into hollow structures known as nanoframes, which retain the surface structure advantages of polyhedral NPs while drastically reducing the amount of inactive Pt atoms. For example, Pt_3Ni nanoframes synthesized from solid Pt-Ni_3 polyhedra demonstrate improved half-cell performance over both commercial Pt/C and Pt-Ni/C catalysts, as well as exceptional durability against voltage cycling [51]. Although they exhibit high activity and stability, nanoframes are difficult to integrate with ionomer and may therefore suffer from proton transport resistance in actual MEAs [6].

In addition to the close-packed NPs described above, one- and two-dimensional Pt nanostructures fall under the category of shape control and can take advantage of specific crystal facets. Such structures include nanosheets/nanoplates, nanowires, nanorods, and nanotubes [16]. Some of these morphologies exhibit properties that may be useful for ORR catalysis. For instance, Pt nanowires can provide high activity through fast electron transfer and exposure of specific crystal facets, and their anisotropic structure leads to high stability [52]. Thus, one- and two-dimensional Pt nanostructures seem promising as a class of catalyst with both high activity and high durability. As with nanoframes, however, much work remains for these to be applied successfully in MEA electrodes.

16

Shape Control

Non-spherical nanoparticles

(100)

(111)

etc.

Other morphologies

Nanoframes

Nanowires

Advantages

$\frac{1}{2}O_2 + 2H^+ + 2e^- \rightarrow H_2O$

High ECSA

High ORR activity (MA, SA)

1 V

0.5 V

High durability

$CO \longrightarrow CO_2$

Good CO oxidation
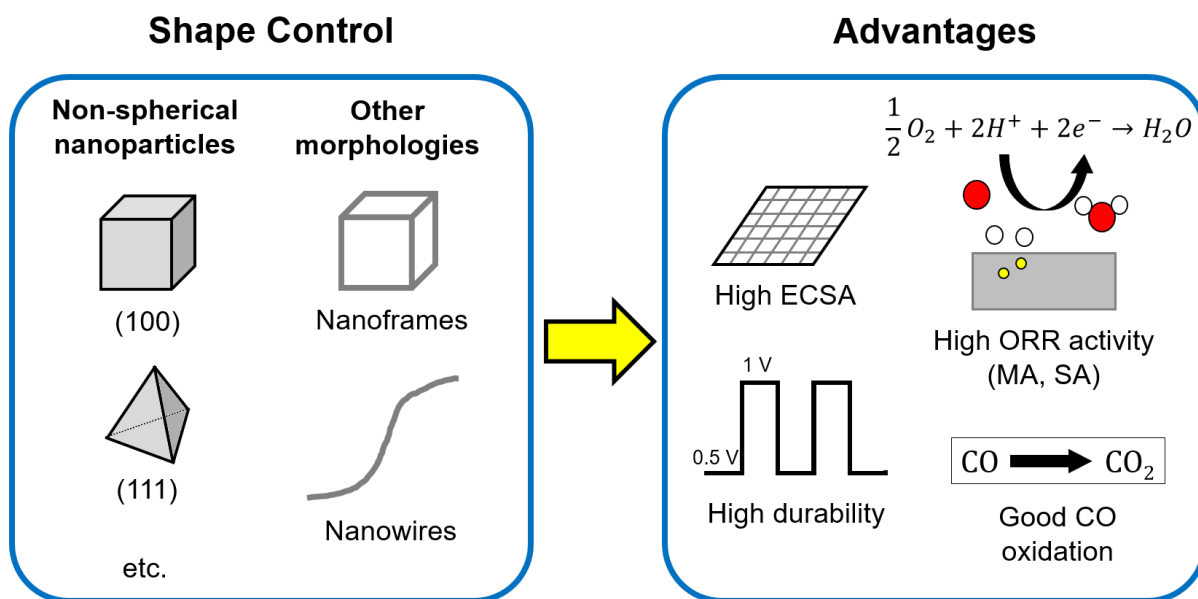
Figure 2.1: Examples of shape-controlled Pt nanostructures and their advantages for PEM fuel cell catalysis

2.2 Carbon-Based Catalyst Supports

2.2.1 Importance of the Carbon Support

While shape-controlled Pt nanostructures are highly promising as PEM fuel cell electro-catalysts, their full potential can only be unleashed with an optimized CL, of which an important component is the catalyst support material. Cathode CL design is recognized as an important pathway towards high current density performance and durability in PEM fuel cells [6]. Among the many challenges encompassed by this topic, optimizing the support material (by either modifying commercial materials or creating new morpholo-

17

gies) appears to be an emerging research focus for next-generation fuel cell technology [7]. Specifically for shaped polyhedral catalysts, an important research area is improving NP size and distribution by optimizing the support material, as this is necessary to maximize fuel cell performance [19]. Moreover, an optimized CL structure can enable high power density and stability with low Pt loading [32], thus reducing the required catalyst cost.

Carbon is commonly selected as the support material for Pt-based electrocatalysts because it promotes catalyst dispersion, stability, and electronic conductivity. Metal NP catalysts require uniform particle size and inter-particle spacing to minimize the rate of particle growth, hence limiting surface area loss and catalyst deactivation [53]. For typical fuel cell catalysts, this is achieved by dispersing Pt NPs on a carbon support with high surface area. Some advantages of carbon over other common catalyst supports are its stability, its resistance to acids and bases, the ability to tailor its pore structure and surface chemistry, and its low cost [54]. Commercial fuel cell electrodes usually employ carbon blacks (e.g., Vulcan carbon, Ketjen Black) [7], which contain varying amounts of micropores to increase their surface area and optimize reactant/product transport. In addition to carbon black, graphitized carbon geometries such as the carbon nanotube (CNT), reduced graphene oxide, graphene nanoplate, and graphite nanofiber can be used in fuel cell electrodes [55]. The carbon support's structure and surface properties affect many phenomena including catalyst dispersion, reaction pathways, activity, and degradation mechanisms [23, 56]. Thus, optimizing the support material is an effective pathway to enhance the catalyst's activity and stability.

The carbon support is also important because it influences the ionomer film distribution. As mentioned in Chapter 1.4, the ionomer conducts protons between the electrodes and electrolyte, and it is essential for forming effective TPBs (i.e., Pt/C catalyst + ionomer

+ gas pores). To achieve this function, the proton-conducting ionomer film must be distributed evenly on the Pt/C surface. Experimental research shows that the adsorption of Nafion, a commonly employed sulfonic-acid-based ionomer, is influenced by both the porosity and surface groups of the support material [57]. Also, the uniformity of Nafion ionomer film is expected to improve when the carbon support is made more hydrophilic via surface functionalization [30]. Uniform ionomer coverage is important for high power density because an uneven distribution can lead to overly thick ionomer in some areas and partial blockages of pores between carbon particles, both of which increase O_2 mass transport resistance [32]. Hence, the effects of carbon support and ionomer on catalyst performance are interdependent, and both should be considered in CL and MEA design.

Experimental studies confirm that the choice of carbon material can impact both the activity and durability of the catalyst. For example, the ORR performance of Pt catalyst has been tested on Ketjen Black, acetylene black, graphene, CNTs, and carbon black, with Ketjen Black giving the highest beginning-of-life MA and acetylene black the best durability against voltage cycling [22]. Another recent study found that Pt and Pt-Co NPs tend to coalesce and lose more ECSA on Vulcan carbon than on more porous carbon blacks (Ketjen, Acetylene Black), but Vulcan carbon is also more resistant to corrosion owing to its higher degree of graphitization [23]. Graphitized materials (e.g., graphene, CNTs) could overcome some of the limitations of carbon blacks, but their integration into actual MEA electrodes remains a challenge. One way to maximize fuel cell performance of graphene-supported catalysts is to combine graphene with carbon black. This allows the carbon black particles to intercalate with graphene, preventing the graphene layers from compacting and maintaining the necessary porous structure for mass transport to the Pt active sites [58, 59, 60]. Carbon materials with tunable porosities, such as accessible mesoporous carbon aerogels [61], can also help optimize the utilization of Pt catalysts.

2.2.2 Functionalization by Oxidation Treatment

One way to improve the carbon support's properties is surface oxidation, which is usually accomplished by treating the carbon in oxidizing acids. This method introduces oxygen-containing surface groups that serve as nucleation sites for metal NPs, ensuring they are well-dispersed and maintain high ECSA [24, 62, 63]. Treating multi-walled CNT supports using a mixture of sulfuric and nitric acids has been observed to enhance both half-cell and single-cell performance of the resulting Pt/C catalyst [24]. However, oxidizing the carbon support also decreases its electrical conductivity, which may partially offset the catalytic advantage from the increased ECSA [63].

The effects of oxidizing acid treatment on Pt/C catalyst performance can be attributed to the modified surface chemistry and microstructure of the carbon support. For instance, the carboxyl groups introduced onto the carbon surface using this treatment are known to increase the carbon's hydrophilicity [64]. This property makes the surface more accessible to aqueous electrolytes, in turn increasing the double-layer capacitance measured in half-cell electrochemical tests [65]. As further evidence of modified surface chemistry, cyclic voltammograms of oxidized carbon show slight peaks in the capacitance region, corresponding to the redox reaction of oxygen-containing surface groups [65]. In addition, atomic force microscope tests suggest that the surface groups increase adhesion between Pt and carbon, enhancing the dispersion and stability of Pt NPs on the support [66]. Another consequence of oxidizing acid treatment is a more electronegative carbon surface, which has been confirmed by measuring the surface zeta potential [67]. Finally, oxidizing acid treatment corrodes the carbon, leading to a degraded porous structure and reduced surface area [63]. This change could possibly affect the size and dispersion of Pt NPs, especially if a one-pot catalyst synthesis method (Chapter 2.3.2) is used.

20

2.2.3 Functionalization by Heteroatom Doping

An alternative to oxidation treatment is doping the support with heteroatoms or functional groups, which can improve Pt dispersion, enhance metal-support interaction, and increase corrosion resistance from high-voltage operation. Nitrogen, boron, and sulfur are examples of dopants that can enhance the activity of supported Pt catalyst in low-temperature fuel cells [7, 68, 69]. These dopants modify the carbon's surface electronic structure and enhance the transfer of electrons between Pt and the support. Nitrogen is a commonly used dopant, and its interaction with Pt atoms varies between the different types of nitrogen defects (e.g., graphitic, pyridinic, or pyrrolic nitrogen) [67, 70]. In actual PEM fuel cells, the presence of positively charged nitrogen-containing species fosters a more uniform surface distribution of ionomer (which contains negatively charged sulfonates), decreasing mass transport polarization and increasing performance at high current densities [32, 71]. In addition to inducing electrostatic effects on Pt catalyst and ionomer, nitrogen doping may affect the carbon support's microstructure. For example, one study on Ketjen Black observes that ammonolysis at 400-600°C etches the carbon and opens up its micropores, increasing its surface area and mesoporosity [32]. However, the change in physical properties of the carbon may vary depending on exactly what nitrogen doping method is used.

Additional strategies have been explored on top of simply adding a single type of functional group to the support material. For instance, Pt NPs on carbon co-doped with nitrogen and nickel benefit from synergistic effects for active sites and metal-support interaction, leading to improved MA and good stability under ORR conditions [72]. Heteroatom doping can also be combined with oxidation treatment, yielding improvements such as good carbon corrosion stability and high ORR specific activity [25, 67]. In addition to doping the support material itself, an alternative approach is to dope a catalyst that already con-

tains metal NPs on the carbon support (e.g., existing Pt/C catalysts). This "post-doping" method improves the durability of Pt/C and Pt-Ru/C catalysts towards fuel cell reactions [73, 74].

2.3 Synthesis of Shape-Controlled Platinum Catalysts

2.3.1 Catalyst Shape Control Strategies

When scaling up a catalyst design into an MEA, the catalyst synthesis method can influence the final catalyst morphology and CL structure, in turn affecting the electrode's performance and stability. This is especially important for shape-controlled Pt NP catalysts, which usually require more complex synthesis methods compared to their spherical or polycrystalline counterparts. Pt NPs are most often synthesized using colloidal methods, which is the focus of this subchapter. Colloidal synthesis is strongly influenced by numerous parameters including the selection of reaction components (e.g., Pt precursor, solvent, reducing agent, stabilizing agent, shape-controlling agent) and conditions (e.g., pH, temperature, pressure, duration of heating) [75].

The colloidal synthesis of shape-controlled Pt NPs involves reacting of a Pt precursor with various agents to control the final particle morphology. The synthesis mechanism can be described in three steps: reduction of the molecular Pt precursor, nucleation of Pt atoms, and growth of Pt NPs [75]. This sequence normally yields the thermodynamically favored product of a given reaction system. In the context of shape-controlled Pt NP synthesis, the thermodynamic product represents the shape with minimum surface free energy. A capping agent or adsorbate (e.g., gaseous environment) is commonly added to

make nanocrystal growth in a specific direction more thermodynamically favorable, thus enabling control of the NP's final shape [33]. Table 2.1 lists some capping agents and stabilizing agents that have been reported in literature for synthesizing shape-controlled Pt-based NPs with controlled low-index facets.

Table 2.1: Capping and/or stabilizing agents that have been used to synthesize shape-controlled Pt and Pt-alloy NPs with low-index crystal facets

Catalyst	Capping and/or Stabilizing Agents	Solvents and/or Reducing Agents	Ref.
Various	Polyvinylpyrrolidone	-	[43]
Pt cubes	KBr	Ethylene glycol, water	[39]
	$Fe(CO)_5$	Octadecene, oleylamine, oleic acid	[20, 37]
	Polyallylamine hydrochloride	Formaldehyde	[35]
	Sodium polyacrylate	-	[20, 43]
	Sodium succinate, peptide sequences, polyvinylpyrrolidone, oleylamine, NaI, $AgNO_3$	-	[20]
Pt tetrahedra, octahedra, and hexagons	Sodium polyacrylate	-	[43]
Pt cub-octahedra	Tetradecyltrimethylammonium bromide	$NaBH_4$	[76]
	$Fe(CO)_5$	-	[77]
Pt octahedra and cuboctahedra	Polyvinylpyrrolidone, $AgNO_3$	Chloroform	[20]

Catalyst	Capping and/or Stabilizing Agents	Solvents and/or Reducing Agents	Ref.
Pt-Ni octahedra	$W(CO)_6$	Oleylamine, oleic acid, benzyl ether	[27]
	Poly(diallyldimethylammonium chloride)	Ethylene glycol	[13, 47]
	Cetyltrimethylammonium bromide	Dimethylformamide	[78]
Pt-Co truncated octahedra	$Mn_2(CO)_{10}$	Oleylamine, oleic acid, benzyl ether	[79]
Pt-Pd octahedra	Polyvinylpyrrolidone	Glycerol	[80]

Sometimes, shape-controlled Pt NPs can be synthesized without adding a strongly adsorbing capping agent or surfactant. Such methods are advantageous because they preserve "clean" Pt surfaces (thus maximizing catalytic activity), minimize complexity and possible imperfections in the synthesis process, and reduce the usage of environmentally unfriendly chemicals. Shape control can be achieved by either generating shape-controlling molecules during the reaction or aiming for a kinetically controlled product (i.e., a product not dictated by the global minimum free energy). Some strategies to synthesize shape-controlled Pt nanostructures without capping agents include controlling the reaction system's temperature and reducing power [81], using certain additives such as KOH [82], and choosing solvents that can generate easy-to-remove stabilizing species during the reaction [40].

In particular, polyols (e.g., ethylene glycol (EG)) have been noted for their utility in surfactant-free synthesis methods [75]. These chemicals are widely used as solvents for Pt catalyst synthesis owing to their high boiling points. Polyol synthesis methods can be

tailored by introducing additional reactants. For example, when NaOH or KOH is added to produce an alkaline environment, the resulting hydroxide ions (OH$^-$) help prevent NPs from agglomerating and govern their growth process. Using this strategy, the molar ratio of OH$^-$ to Pt can be controlled to tune the final NP size [83, 84]. Another example of a modified solvothermal synthesis method is adding N,N-dimethylformamide (DMF) as a co-solvent along with EG. DMF by itself acts as a solvent and reducing agent in the synthesis of Pt-based NPs with cubic, octahedral, and similar morphologies [85, 86]; when combined with EG and KOH, it can help produce other structures such as Pt nanowires [87]. With further efforts in scaling up the reaction system and simplifying the synthesis procedure, this class of solvothermal synthesis methods is a promising pathway towards low-cost production of shape-controlled Pt nanostructures.

2.3.2   Scalable Catalyst Synthesis Methods

The ability to synthesize shape-controlled Pt nanostructures in large quantities is essential for translating them into cost-effective fuel cell catalysts. Novel Pt-based catalysts are usually synthesized in batches containing no more than a few dozen mg Pt. While such a quantity is enough for material characterization, it is hardly sufficient for MEA testing, let alone commercial-scale production [27]. Colloidal catalyst synthesis methods can be scaled up by either simply increasing the batch size or switching to a continuous production method. There are some studies in literature, such as our group's previous work [88], reporting high-performing fuel cell catalysts produced in large batches. However, this approach may be confounded by challenges such as large thermal gradients, poor batch-to-batch reproducibility, and chemical safety/waste concerns [89]. An alternative is the continuous-flow droplet reactor, which separates the reactants into small droplets with more

uniform thermal gradients. This method can be applied to synthesize Pt-Ni octahedral NPs at 20 mg/hour, with higher rates possible if multiple microfluidic devices are run in parallel [27]. A similar method with atomized droplets on a conveyor transport system is capable of synthesizing shaped Pt-Ni NPs supported on carbon black [90]. However, continuous-flow droplet systems face their own challenges such as reaction duration, carrier phase, flexibility in how multiple reagents are mixed, and continuous monitoring [89]. Regardless of whether the batch-based method or continuous-flow droplet reactor is used, effective and reproducible production remains a major hurdle for the application of high-activity Pt catalysts.

Furthermore, the synthesis of shape-controlled catalysts in large quantities requires careful control of conditions for the synthesis process, so shape-controlled Pt/C catalysts are typically synthesized in two steps. The first step is to synthesize the shape-controlled Pt NPs, and the second is to deposit these NPs onto the functionalized carbon support [28]. This physical mixing process may fail to bond the Pt NPs strongly to the carbon support, adversely affecting the catalyst's stability [28]. The multi-step process also decreases the productivity and increases the cost associated with manufacturing of Pt/C catalysts for commercial applications. In contrast, one-pot (also called one-step) synthesis is a single reaction between Pt precursor and carbon support that directly forms carbon-supported Pt catalyst. The one-pot approach is advantageous in terms of simplicity and low cost [35, 50], which can help minimize both material and fabrication cost of advanced PEM fuel cell catalysts. However, the interactions between Pt nuclei and the carbon support influence morphology control of Pt NPs, and such influences may be problematic if they hinder the synthesis of regularly shaped non-spherical NPs [35, 76]. Nevertheless, one-pot synthesis methods have been used successfully for shape-controlled Pt catalysts. For example, several research groups have adapted the previously described method with EG, DMF, and KOH

into one-pot methods, yielding carbon-supported nanowires [52], tetrahedra [40, 49, 91], octahedra [91], or nanocubes [92]. Another interesting method is to use premade Pt/C catalyst instead of carbon in the one-pot system and deposit new Pt atoms onto the existing NPs. Using bromide ions for shape control, this method yields small and surfactant-free Pt nanocubes with enhanced electrocatalytic activity [93].

One-pot synthesis development is complicated by the adoption of functionalized carbon supports. Some functional groups affect the formation of Pt nuclei on the support, impacting Pt NP growth. If the Pt precursor and carbon surface are similarly charged (i.e., both are positive or negative), then the Pt precursor groups tend to repel from the surface, making it more difficult to form highly dispersed NPs on the support. An example of this case would be $PtCl_6^{2-}$ and oxidized carbon [54]. The problem can be solved by choosing a precursor that forms an oppositely charged intermediate; for example, $Pt(NH_3)_4^{2+}$ would theoretically work better with oxidized carbon. However, changing the Pt intermediate may alter its interaction with other species in the reaction system depending on the synthesis method used, and ultimately, doing so does not necessarily improve the Pt NP size and dispersion [83]. Heteroatom dopants, such as nitrogen and sulfur, can also influence the Pt nucleation and growth processes, impacting the final NP size [69]. Continued exploration of one-pot synthesis is needed to determine how to combine shape-controlled Pt NPs with functionalized carbon materials to create highly active and stable catalysts.

2.4 Performance of Shape-Controlled Platinum-Based Catalysts in PEM Fuel Cells

Even if a catalyst performs well and can be synthesized in a controlled manner, its performance in PEM fuel cells is still affected by various factors related to CL and MEA fabrication. To prepare the anode and cathode electrodes on an MEA, a catalyst ink is prepared by mixing Pt/C catalyst with an ionomer solution and a solvent, and the ink is coated onto a substrate (i.e., a PEM, GDL, or decal) and dried. All of these steps have been found to affect the final CL structure and, subsequently, fuel cell performance [15, 94, 95, 96, 97, 98, 99]. Furthermore, design parameters such as catalyst loading (mg_{Pt}/cm^2) and MEA size can affect the fuel cell's overall performance and cost. Pt loading is important to consider because reducing Pt loading leads to lower MEA cost, but possibly at the expense of performance and durability. According to recent research, PEM fuel cells with low Pt loading often perform poorly because of local O_2 transport resistance at the ionomer interfaces [11, 100]. The MEA active area is also influential because single-cell testing on a large cell introduces heat and water management challenges on top of electrochemical effects [101]. Although optimizing all these factors is beyond the scope of this thesis, their impacts need to be recognized when designing catalysts for practical PEM fuel cell usage.

A limited number of single-cell experiments has been conducted for non-spherical and carbon-supported Pt catalysts, as summarized in Table 2.2. Experimental details such as the MEA's Pt content and operating conditions are provided because they can impact single-cell test results.

28

Table 2.2: MEA performance of non-spherical Pt and Pt-alloy catalysts with carbon supports. All tests used Nafion ionomer and H_2/air unless otherwise specified.

Catalyst	Support	Cathode Pt content [mg/cm^2]	Voltage	Peak Power [W/cm^2]	Durability	Ref.
Non-spherical Pt NPs	High-area carbon (treated with oxidizing acids)	0.4	Up to 0.7 A/cm^2 at 0.7 V	Up to 1.1	As low as 5% loss at 1.1 A/cm^2 after 30000 cycles at 0.6-1 V	[88]
Pt-Ni octahedra	Ketjen Black ECP-600JD	0.14	0.39 A/cm^2 at 0.8 V	-	No loss after 10000 cycles at 0.6-0.9 V	[47]
	Carbon black	0.4	Up to 0.712 V at 1 A/cm^2	0.882	7% loss at 1 A/cm^2 after 100 h at 1 A/cm^2	[13]
	Vulcan XC-72	0.4	0.683 V at 1 A/cm^2	0.965	6.9% loss at 1 A/cm^2 after 100 h at 1 A/cm^2	[102]
Pt-Ni octahedra	CNT	0.4	0.643 V at 0.6 A/cm^2	0.433	3.6% loss at 1 A/cm^2 after 1 h at 1.5 V	[78]
Pt-Ni octahedra	BP2000 carbon black (graphitized at 1600-2200°C)	0.4	Up to 0.672 V at 1 A/cm^2	Up to 0.818	As low as 3.9% loss at 1 A/cm^2 after 1 h at 1.4 V	[103]

Catalyst	Support	Cathode Pt content [mg/cm^2]	Voltage	Peak Power [W/cm^2]	Durability	Ref.
Pt-Co truncated octahedra	Ketjen Black	0.1	-	0.702	4.1% max. power loss after 30000 cycles at 0.6-0.95 V	[79]
Pt cuboctahedra	Vulcan carbon or CNT	0.21	-	Higher than Pt/C, per mg$_{Pt}$ (H_2/O_2)	-	[76]
Pt nano-dendrites	Vulcan XC-72R	0.2	Up to 0.952 A/cm^2 at 0.6 V (H_2/O_2)	-	-	[104]
Pt nanowires	Multimodal porous carbon (with graphitic carbon nitride)	0.13	-	Up to 0.570	-	[105]

Some shape-controlled Pt and Pt-alloy catalysts with carbon supports seem to perform well on the MEA scale. As an example, an octahedral Pt-Ni catalyst with Ketjen Black carbon support has demonstrated similar performance at 0.14 mg$_{Pt}$/cm^2 as commercial Pt/C at 0.5 mg$_{Pt}$/cm^2, indicating an improvement in the catalyst's Pt utilization [47]. In a different study, octahedral Pt-Ni/C catalyst is introduced into an MEA using carbon black with 0.4 mg/cm^2 Pt loading, achieving a nearly quadruple exchange current

density compared to commercial Pt/C and a peak power density of 0.882 W/cm^2 [13]. Other catalyst morphologies, including Pt-Co truncated octahedra, Pt cuboctahedra, Pt nanodendrites, and Pt nanowires, demonstrate comparable or improved single-cell performance relative to commercial Pt/C. Changing the carbon support properties can help optimize the fuel cell performance of such shape-controlled Pt NP catalysts. For example, one research group conducted multiple studies on Pt-Ni octahedra using Vulcan carbon, CNTs, and graphitized carbon blacks, revealing a trade-off between activity and durability [78, 102, 103].

CL optimization is recognized as an important research area for shape-controlled Pt-based catalysts [19]. For example, in a study on Pt nanodendrite catalyst, the choice of a catalyst-coated membrane vs. catalyst-coated substrate MEA fabrication method is observed to impact MEA performance greatly [104]. In a different study on a Pt nanowire-like catalyst, a multimodal porous carbon support with small amounts of graphitic carbon nitride is found to improve MEA performance [105]. However, the authors postulate that optimization of the catalyst ink and CL fabrication process is still required to achieve high power density with this nanowire catalyst [105]. Finally, the research group who published multiple studies on Pt-Ni octahedra found that using CNT as the support causes the CNTs to intertwine and reduce contact between ionomer and active components, leading to poor fuel cell performance [78].

Another important consideration is that operating conditions such as temperature, relative humidity (RH), and reactant flow rate can noticeably affect single-cell performance. Most of the voltages and peak power densities reported in Table 2.2 are recorded in well-humidified conditions, but the DOE's 2020 fuel cell performance targets specify a harsher condition of 40% RH (59°C dew point at 80°C dry bulb temperature) [18]. Thus, the peak

31

power densities recorded by all these studies might not be achievable in all practical operating conditions. An emerging research area that can address this problem is alternative ionomer materials, which may improve water management and low-RH performance.

2.5 Experimental Characterization of Fuel Cell Catalysts

2.5.1 Physical Characterization

Physical testing provides information on catalyst composition and morphology, and it is an important component of experimental studies. Some techniques commonly used in PEM fuel cell catalyst research include X-ray diffraction (XRD), Brunauer-Emmett-Teller (BET) surface area measurement, scanning electron microscopy (SEM), transmission electron microscopy (TEM), thermogravimetric analysis (TGA), and X-ray photoelectron spectroscopy (XPS) [106]. One study on cubic and octahedral Pt alloy NPs [107] illustrates some of these characterization techniques. The authors use TEM to image individual NPs, SEM with energy dispersive X-ray spectroscopy to analyze their elemental composition, and XRD to identify crystal planes. XRD can also be used to calculate the average NP size using the Scherrer equation [106]. TGA is useful for estimating the Pt weight percentage of Pt/C catalysts, and BET analysis can be used to measure their specific surface areas [108]. Furthermore, X-ray absorption spectroscopy is capable of determining the electronic structure (e.g., oxidation states) and local coordination of Pt atoms [75], and this information has been used to compare the degradation mechanisms of different electrocatalysts [109].

2.5.2 Electrochemical Characterization

Half-cell testing is frequently employed in experimental fuel cell studies to quickly characterize the performance and durability of a catalyst design. In fuel cell research, cyclic voltammetry (CV) is typically conducted to obtain the catalyst's H_2 electro-adsorption charge value, which is used to calculate ECSA. Subsequently, linear sweep voltammetry (LSV) is conducted to measure the ORR performance with different rates of ion transport, revealing the catalyst's kinetic current and limiting current densities [106]. The kinetic current is used to obtain MA measured at a specified potential, and this result is substituted (alongside ECSA) into Equation 1.5 to calculate SA. Half-cell testing is also frequently used to evaluate cell durability using an accelerated stress test protocol such as potential cycling. The most ubiquitous half-cell test setup is the rotating disk electrode (RDE), which uses a three-electrode configuration with a working electrode, counter electrode, and reference electrode, all of which are immersed in an aqueous electrolyte. During the test, the working electrode containing Pt/C catalyst is rotated to provide ion transport from the electrolyte via forced convection [106].

The selection of electrolyte and ionomer may impact the ORR activity of shape-controlled Pt catalysts in half-cell tests. Sulfonate anions (e.g., those present in Nafion ionomer) are known to adsorb more strongly onto Pt(111) than Pt(100), so the relative performance of Pt(111) depends on whether it is used in a weakly or strongly adsorbing electrolyte. For instance, Pt(111) shows relatively high performance in perchloric acid but low performance in sulfuric acid [16]. There is some uncertainty about which type of electrolyte (e.g., perchloric vs. sulfuric acid) best represents the catalyst's performance in a PEM fuel cell [7]. In addition, an ionomer is normally used in half-cell tests to help create well-dispersed catalyst inks, but it may hinder ORR activity because of anion ad-

sorption on the catalyst. The effect of ionomer is particularly important for catalysts with a low Pt-to-carbon weight ratio [110]. Thus, half-cell results for different catalysts might not be directly comparable unless they are tested using the same electrolyte and ionomer type/quantity.

Relative to single-cell testing, the RDE method is simpler and measures inherent catalytic activity more directly, but it fails to reflect the higher Pt loading, harsher operating conditions, higher current density, and more limited mass transport in real PEM fuel cells [30]. These limitations help explain why the exceptional RDE performance of advanced fuel cell catalysts, such as Pt alloys and shape-controlled nanostructures, does not necessarily correlate with good MEA performance.

2.5.3   Fuel Cell Testing

Single-cell testing in an MEA provides the most accurate assessment of a catalyst's performance in practical PEM fuel cell conditions. As described briefly in Chapters 2.3 and 2.4, single-cell preparation involves synthesizing Pt/C catalyst, combining Pt/C with ionomer in a catalyst ink, depositing this ink onto a substrate such as a PEM, and combining the electrodes with a PEM and two GDLs to create an MEA. Following this, the MEA is evaluated using a test station, which supplies fuel and oxidant to the MEA while controlling parameters such as temperature, humidity, reactant flow rates, coolant supply, current, and voltage [106]. The test yields a polarization curve, which reveals the activation, ohmic, and mass transport performance losses in the MEA. During a test, in-situ prognosis of MEA degradation can be conducted by monitoring the voltage and temperature, conducting electrochemical impedance spectroscopy, or running an accelerated stress test [111]. MEAs can also be tested inside an environmental chamber to simulate practical challenges, such as

cold start-up from approximately -3 to -7°C [112]. Like RDE testing, MEA testing can provide information on the catalyst's activity and durability, but it also involves unique challenges such as water flooding, mechanical degradation of the PEM and CL, and so forth.

During a single-cell test, operating conditions such as temperature, RH, reactant stoichiometry, and pressure have a twofold effect on MEA performance. First, these conditions affect the reversible cell potential as described by the Nernst equation, which predicts reversible potential as a function of temperature and reactant partial pressures. Second, the operating conditions impact the activation, ohmic, and mass transport overpotentials through a wide range of mechanisms. Experimental and theoretical studies indicate that MEA performance generally improves with inlet gas temperature and RH because of their effect on PEM conductivity [113]. However, at high RH, thin porous cathode CLs are more prone to flooding [114], and CLs with many micropores (<2 nm) may suffer from water accumulation promoted by capillary forces [115]. As another example, high reactant flow rate (or stoichiometry) has been observed to be favorable for MEA performance in fully humidified conditions, but it becomes unfavorable in low humidity conditions because of the resulting ionomer and membrane dehydration [101].

2.6 Contributions of Thesis

To help advance the adoption of shape-controlled Pt catalysts in PEM fuel cells, this thesis work develops and characterizes a non-spherical Pt NP catalyst supported on different functionalized carbon supports. A high-surface-area carbon black material is functionalized by either oxidizing acid treatment or nitrogen doping, and these carbon varieties are used in

a one-step solvothermal synthesis method with EG, DMF, and NaOH designed to facilitate the formation of shape-controlled Pt NPs. The effects of carbon support functionalization on non-spherical Pt catalyst are deduced using conventional physical and electrochemical tests. Furthermore, the synthesis procedure is repeated using both small and large batches to investigate its suitability as a scaled-up synthesis process. This addresses a gap in the current literature, which lacks detailed findings on how scaling up a batch-based one-pot synthesis method may impact the catalyst's size/morphology and its electrochemical performance.

2.7   Summary

Shape-controlled Pt nanocrystals hold much promise as high-activity fuel cell catalysts, but their full potential can only be realized with scalable catalyst synthesis procedures and optimal MEA design. Various morphologies have been found to enhance the activity and robustness of Pt-based catalysts, leading to higher ECSA, SA, and MA towards the ORR. These catalysts are further improved by appropriate selection and functionalization of the carbon support, whose microstructure and surface chemistry can influence the Pt catalyst properties. The benefits of both non-spherical Pt catalysts and functionalized carbons have been verified experimentally. Nevertheless, non-spherical Pt catalysts have not substantially improved the utilization and lifetime of PEM fuel cell catalysts on a commercial scale. To accomplish this, more research is needed into simplified and scaled-up catalyst synthesis methods (particularly one-pot methods), coupled with optimized CL fabrication and design. The ultimate goal for fuel cell applications is to achieve high peak power density, high durability, low cost, and robustness against varying operating conditions.

In this study, a non-spherical Pt catalyst is synthesized with both oxidized and nitrogen-doped carbon to study the effects of carbon functionalization, and then the one-pot synthesis method is repeated in both small and large batches to evaluate how scalable the catalyst performance is. Physical and electrochemical tests are used to characterize the catalyst samples. This work contributes to the usage of shape-controlled Pt catalysts in practical PEM fuel cell applications.

Chapter 3

Experimental Methods

3.1   Materials and Chemicals

Ketjen Black EC-600JD carbon powder (AkzoNobel), hydrochloric acid (37%, Sigma-Aldrich), sulfuric acid (95-98%, Sigma-Aldrich), nitric acid (70%, Caledon Laboratories), chloroplatinic acid hexahydrate ($\geq 37.50\%$ Pt basis, Sigma-Aldrich), ethylene glycol (Fisher Scientific), N,N-dimethylformamide ($\geq 99.8\%$, Sigma-Aldrich), sodium hydroxide ($\geq 97.0\%$, Sigma-Aldrich), ethanol (HPLC, Sigma-Aldrich), Nafion (5% solution, Ion Power), and perchloric acid (70%, GFS Chemicals) are used as received. Nitrogen (99.998%), argon (99.998%), and oxygen (99.993%) compressed gas cylinders are obtained from Linde. Deionized water is supplied from our laboratory.

3.2 Carbon Treatment and Functionalization

3.2.1 Hydrochloric Acid Treatment

All of the carbon supports used in this work are pre-treated using hydrochloric acid. To begin this process, 6 g of Ketjen Black EC-600JD carbon is mixed with 800 mL of 2.5 M hydrochloric acid inside a round-bottom flask. The flask is submerged in a silicone oil bath atop a hot plate, and the mixture is refluxed at 120°C for 18 hours with magnetic stirring. A straight tube condenser with running water is attached to the flask to prevent loss of liquid by evaporation. Then, the mixture is left to cool overnight, allowing the carbon to precipitate from the mixture. After removing the clear liquid, the product is transferred into 50 mL centrifuge tubes using deionized water (DIW), and the tubes are rotated at 3400 rpm for 20 minutes to collect the product.

Following this, the carbon is transferred back into the flask, mixed with 800 mL of DIW, and refluxed at 120°C for 8 hours. The centrifuge wash/separation process is repeated 3-4 times until the sample is approximately pH-neutral. Finally, the carbon is dried inside a temperature-controlled chamber at 85°C, ground into powder, and collected into glass vials.

3.2.2 Functionalization

To prepare carbon functionalized by oxidizing acid treatment, 2 g of the HCl-treated carbon is mixed with 67 mL of 4 M sulfuric acid and 200 mL of 4 M nitric acid. The mixture is refluxed at 120°C for 4 hours with magnetic stirring as described above. Thereafter, the product is washed and collected by centrifugation as described above.

To prepare carbon functionalized by nitrogen doping, 1.6 g of the HCl-treated carbon is dispersed in 100 mL of DIW, and 5 g dicyanamide is dissolved in 40 mL of hot DIW. The two mixtures are stirred for 30 min and then heated at 180°C for 20 hours in an autoclave, before collecting the carbon and washing repeatedly with DIW. Afterwards, the carbon is mixed in 75 mL ammonium hydroxide, heated again at 180°C for 20 hours, and washed again. Finally, the carbon is treated in N_2 gas at 900°C to obtain the final product.

In this thesis, the carbon supports are named based on the carbon functionalization method. The carbon supports that are non-functionalized (i.e., treated with only HCl), oxidation-treated, and nitrogen-doped are called KB, KB-O, and KB-N, respectively (Figure 3.1).
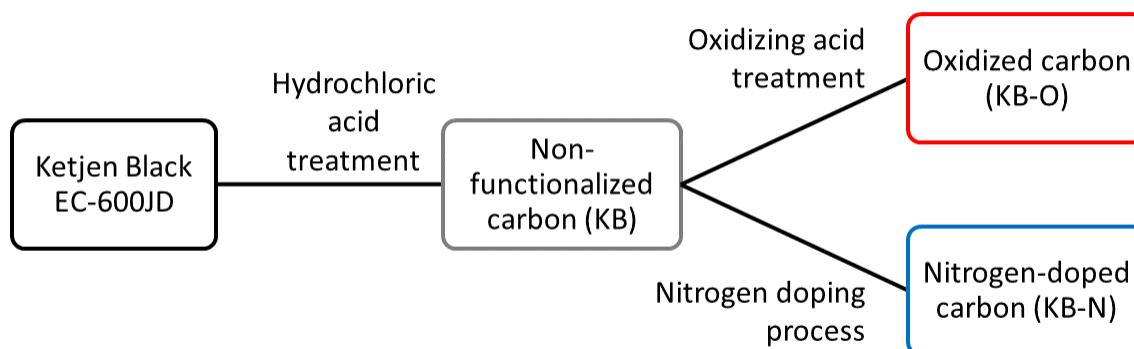

Figure 3.1: Summary of the three carbon supports prepared in this study

3.3 Catalyst Synthesis

To obtain non-spherical Pt NPs supported on carbon, a modified one-pot solvothermal synthesis method similar to those reported by Rana et al. [40], Xia et al. [92], Hoque et al. [52], and others is adopted. This method is selected because it generates shape-directing species from reactions between DMF and OH$^-$, and these species can easily be removed using a water/ethanol wash process. The ratio of Pt precursor to carbon is controlled for a nominal Pt content of 48.5 wt.%, which is based on our group's previous work indicating that catalysts with high Pt content (60 wt.%) tend to outperform those with low Pt content (20 wt.%) in single-cell tests [29].

In a typical synthesis, 600 mg of NaOH pellets, 8 mL of EG, and 12 mL of DMF are added to a round-bottom flask. The mixture is magnetically stirred at room temperature for several hours to dissolve the NaOH. Thereafter, 100 mg of H$_2$PtCl$_6$ · 6H$_2$O is added to the flask and the mixture sonicated for 20 min, and then 40 mg of carbon (KB, KB-O, or KB-N) is added and the mixture sonicated for another 20 min. After magnetically stirring the mixture overnight at 200 rpm, the flask is submerged in a silicone oil bath atop a hot plate, and the mixture is heated at 170°C for 8 hours. While heating the mixture, a condensing tube with cooling water is attached to the flask, and any open necks on the flask are blocked using stoppers. A small flow of inert gas (nitrogen or argon) is supplied through the top of the condensing tube. Afterwards, the flask is removed from the heat source for natural cooling to room temperature, at which point the cooling water and inert gas flows are shut off.

To collect the catalyst, the mixture is transferred into a 50 mL centrifuge tube, filled with DIW, and separated at 3400 rpm for at least 20 min. After the clear top liquid is removed, a water/ethanol wash is performed by adding approximately 5 mL of ethanol, filling

41

the rest of the tube with DIW, shaking the tube to disperse the catalyst, and centrifuging for another 20 min. This wash process is repeated 3-4 times to remove any residual surfactants and chemicals from the synthesis process. Once the washing is complete, the product is transferred into an evaporation disk using DIW and dried in air for at least 48 hours. Finally, the product is transferred into a crucible and placed inside a temperature-controlled chamber at 70°C for 24 hours before collection into a glass vial.

To scale up the synthesis procedure, everything described above is repeated but with all reactant quantities scaled up tenfold (i.e., using 1 g of $H_2PtCl_6 \cdot 6H_2O$). The only differences are usage of a larger round-bottom flask (500 mL) and multiple centrifuge tubes / larger evaporation disks.

In this study, the catalyst names indicate which carbon support they contain (KB, KB-O, or KB-N) and whether they are synthesized in small or large scale (1x or 10x). The small-scale catalyst samples on KB, KB-O, and KB-N are referred to as Pt/KB, Pt/KB-O, and Pt/KB-N, respectively; the corresponding large-scale samples are referred to as Pt/KB-10x, Pt/KB-O-10x, and Pt/KB-N-10x, respectively.

3.4   Physical Characterization

3.4.1   Carbon Support Characterization

BET area measurements of the carbon powders are taken using a Micromeritics Gemini VII 2390a machine to estimate their surface areas. Each sample (approx. 100 mg) is degassed in a nitrogen atmosphere at 300°C to remove any residual water and impurities.

For the surface area measurement, the sample tube is immersed in a liquid nitrogen bath, and nitrogen gas is used as the adsorbate. The test yields a plot of amount of gas adsorbed (Q) vs. relative pressure (P/P_0), which is analyzed by applying the BET equation:

$$\frac{P/P_0}{Q(1 - P/P_0)} = \frac{1}{Q_m C} + \frac{C-1}{Q_m C}\frac{P}{P_0} \tag{3.1}$$

where P is pressure, P_0 is saturated vapor pressure, Q is amount of adsorbate molecules added (in mol), Q_m is amount of molecules corresponding to a monolayer on the sample (in mol), and C is a constant. When P/P_0 is approximately 0.05-0.30, plotting the left side of the equation vs. P/P_0 gives a straight line, from which Q_m can be calculated. The sample's specific BET area is then determined as:

$$S_{BET} = \frac{Q_m N A_{cs}}{m} \tag{3.2}$$

where S_{BET} is specific BET surface area (in m^2/g), N is Avogadro's number, A_{cs} is cross-section area of one adsorbate molecule (0.162 nm^2 for N$_2$ [116]), and m is mass of the sample.

XPS measurements are taken using a VGS ESCALab 250 Imaging ESCA system to study the surface chemistry of the three carbon supports. This technique measures the intensity of ejected electrons as a function of their binding energies, with specific binding energies corresponding to specific electrons in a given element. Thus, the elemental composition of a material and the bonding information of these elements can be examined (C, O, and N are the most important in this work). A survey measurement (0-1200 eV) is

captured for each sample, followed by C 1s, O 1s, and N 1s spectra. Binding energy is calculated using the Einstein relation:

$$E_b = h\nu - E_k \tag{3.3}$$

where E_b is binding energy, $h\nu$ is a constant based on the X-ray source (1486.68 eV), and E_k is kinetic energy (measured by the analyzer).

3.4.2   Pt/C Catalyst Characterization

TEM images of the catalyst samples are captured using a Zeiss Libra 200 MC system operating at 200 kV. A range of magnification values (50kx, 100kx, 200kx, 400kx) is used to observe the Pt NP size, morphology, crystallinity, and distribution on the carbon support. At least two locations are observed for each sample to ensure that the captured images accurately represent the entire sample. NP size distributions are estimated by manually measuring 200-300 particles from at least two different 200kx images.

TGA measurements are conducted on the catalyst samples to estimate their mass fractions of Pt. A TA Instruments TGA Q500 machine is used with air as the purge gas, and approximately 7-10 mg of each catalyst sample is loaded into a Pt pan. The machine is programmed with a ramp rate of 40°C/min between room temperature and 300°C, 10°C/min between 300-525°C, and 40°C/min between 525-725°C. (Some samples tend to oxidize at higher or lower temperatures, so the temperatures are adjusted such that most of the oxidation occurs in the 10°C/min period.) As the temperature transitions from room temperature to above 700°C, any water inside the sample or on the pan evaporates, and

the carbon support oxidizes in the air atmosphere. The changes in total sample weight reveal the mass fractions of Pt, carbon, and water, assuming these are the only significant components in the sample. By comparing the sample mass at approximately 200°C (after the water evaporates) vs. 700°C (after the carbon oxidizes), the catalyst's Pt content is calculated as:

$$L_{Pt} = \frac{m_{Pt}}{m_{Pt} + m_{carbon}} = \frac{m_{total} \text{ at } 700°C}{m_{total} \text{ at } 200°C} \tag{3.4}$$

where L_{Pt} is Pt mass fraction on the sample in wt.%.

Powder XRD patterns are obtained to characterize the crystallographic structure of the catalysts and estimate their mean NP size [106]. For each of the large-scale catalyst samples, a full scan measurement is taken to characterize the overall crystalline structure, followed by a detailed scan of the Pt(111) peak to determine the mean NP size via peak broadening. The full scan is taken using a Rigaku Miniflex II machine between $2\theta = 20$-$90°$ with a step size of 0.05°. The detailed peak scan is taken using a Bruker D8 machine between $2\theta = 37$-$43°$ with the same step size at a slower scan rate. The Scherrer equation is used to calculate mean crystallite size:

$$\tau = \frac{0.9\lambda}{\beta \, cos\theta} \tag{3.5}$$

where τ is crystallite size, λ is wavelength of the X-ray beam (0.154 nm for Cu Kα radiation), β is peak broadening based on full width at half maximum of the 2θ plot (in radians), and θ is incident angle corresponding to the Pt(111) peak. The slow scan rate for the detailed scan minimizes the instrumental contribution to β.

45

3.5   Electrochemical Characterization

Half-cell (ex-situ) electrochemical characterization is performed on an RDE system to measure the catalysts' ORR performance and properties. For each test, 5 mg ($\pm$ 0.2 mg) of the catalyst sample is weighed inside a 20 mL glass vial using a microbalance. 0.5 mL DIW, 4.5 mL ethanol, and 30 μL Nafion solution are added to the vial, with the amounts adjusted proportionally if the actual measured weight of catalyst deviates from 5 mg. Then, the contents are sonicated inside a water bath for 25-30 minutes to form a homogeneous catalyst ink.

RDE tests are conducted using a rotating disk electrode system (BAS RRDE-3A) and electrochemical instrument (CH Instruments 760E). In a conventional three-electrode cell setup, a glassy carbon electrode (4 mm diameter) is used as the working electrode, a reversible hydrogen electrode (RHE) as the reference electrode, a Pt wire as the counter electrode, and 0.1 M perchloric acid as the electrolyte. Prior to each test, the working electrode is sonicated in DIW and polished using alumina to ensure a clean and smooth surface. To load the catalyst sample, the ink is cast onto the working electrode using a micropipette, and the electrode is rotated at 100 rpm in ambient air to fully evaporate the solvents. The ink volume is controlled at 6.4 μL (cast in two drops of 3.2 μL each), corresponding to approximately 24 μg$_{Pt}$/cm^2. Once the ink is dry, the working electrode is immersed into the electrolyte and inspected to ensure no bubbles form on the surface. Nitrogen or oxygen gas is supplied to the electrolyte according to the test sequence. All tests are conducted at room temperature (around 21.5°C). To ensure repeatability of the results, each catalyst sample is tested with at least 3 inks, with multiple measurements taken for each ink.

CV curves are measured to determine the catalyst's ECSA based on its hydrogen des-

orption charge. The electrolyte is saturated with N_2 by purging the setup with N_2 gas. 50 potential cycles are run between 0.05-1.2 V (vs. RHE) using a scan rate of 0.5 V/s to activate the catalyst and observe preliminary data. Then, 5 cycles are run between the same potentials at 0.1 V/s to collect the actual data. The H_2 desorption peak area from the final cycle is used to calculate the catalyst's ECSA as follows:

$$\text{ECSA} = \frac{Q_{des}}{(210 \times 10^{-6} \ C/cm^2) \times m_{Pt}} \tag{3.6}$$

$$Q_{ads} = \int I \, dt = \frac{1}{v} \int_{V_1}^{V_2} I \, dV = \frac{1}{v} \times \text{area} \tag{3.7}$$

$$m_{Pt} = m_{Pt/C,ink} \times L_{Pt} \times \frac{V_{electrode}}{V_{ink}} \tag{3.8}$$

where Q_{des} is the catalyst's H_2 electro-desorption charge, v is scan rate (in V/s), "area" refers to the hydrogen desorption peak on the CV graph (using the current at 0.4 V as the baseline), m_{Pt} is mass of Pt on the test electrode, $m_{Pt/C,ink}$ is mass of catalyst in the batch of catalyst ink, L_{Pt} is Pt loading on the catalyst sample (in wt.%), $V_{electrode}$ is volume of ink that was cast onto the test electrode, and V_{ink} is total volume of the batch of catalyst ink.

LSV is conducted to measure the catalyst's ORR activity, which is quantified by MA and SA. Measurements are taken in both N_2- and O_2-saturated electrolyte, with the electrolyte purged for at least 1 hour every time the gas is changed. Current density is measured from 0.1-1.2 V (vs. RHE) in the positive direction with a scan rate of 0.02 V/s, with rotation speeds of 800, 1200, 1600, 2000, and 2400 rpm. Background noise correction is accomplished by subtracting the LSV curves measured using N_2 from those using O_2 at

the same rotation speed. The corrected data is then used to calculate ORR kinetic current as described by the Koutecky-Levich equation:

$$\frac{1}{I} = \frac{1}{I_D} + \frac{1}{I_K} \tag{3.9}$$

where I is total current measured by the test station, I_D is diffusion-limited current due to ion transport, and I_K is kinetic current (which is a function of potential). At low potentials, the reaction is diffusion-limited and I (measured at 0.3 V) is approximately equal to I_D. Substituting this value for I_D and I (at 0.9 V) into the Koutecky-Levich equation yields I_K (at 0.9 V). The measurement of I_K at 0.9 V is consistent with the DOE's performance targets for fuel cell electrocatalysts [18]. Finally, the catalyst's MA and SA are calculated as:

$$\mathrm{MA} = \frac{I_K}{m_{Pt}} \tag{3.10}$$

$$\mathrm{SA} = \frac{\mathrm{MA}}{\mathrm{ECSA}} \tag{3.11}$$

An accelerated stress test (AST) is conducted to study the catalyst's durability against potential cycling, which is important for fuel cell applications requiring frequent voltage transients (e.g., automotive). Catalyst degradation is accelerated by repeatedly oxidizing and reducing the catalyst surface while avoiding corrosion of the carbon support [18]. The working electrode potential is cycled 20,000 times between 0.5-1 V (vs. RHE) using a scan rate of 0.5 V/s under N_2-saturated conditions. CV is measured at 0.1 V/s after every 500-1000 cycles to determine the change in ECSA resulting from the AST. In this study, the durability test between 0.5-1 V is called the "catalyst AST".

Furthermore, to observe catalyst degradation from corrosion of the carbon support, the AST is repeated as above but with the potential cycling between 1-1.5 V (vs. RHE) for 5,000 cycles. This potential range is consistent with that specified by the DOE for fuel cell electrocatalysts [18]. While PEM fuel cells are unlikely to encounter such high voltages on a regular basis, they may still occur if the fuel cell starts up or shuts down in an unmitigated manner [18]. In this study, the durability test between 1-1.5 V is called the "corrosion AST".

Chapter 4

Results and Discussion

4.1 Carbon Support Properties

4.1.1 BET Surface Area

Figure 4.1 shows the BET surface areas of KB, KB-O, and KB-N, which are estimated to be 1101, 924, and 1305 m^2/g, respectively. These discrepancies confirm that functionalizing Ketjen Black carbon affects its physical properties, which in turn could affect the deposition of Pt NPs during one-pot catalyst synthesis. For KB-O, the loss of BET area confirms previous results in literature, which indicate that oxidation treatment degrades the porous structure and decreases BET area (Chapter 2.2). For KB-N, the increase in BET area could be explained by an etching and opening of the Ketjen Black carbon's porous structure, similar to a previous study also using Ketjen Black [32].
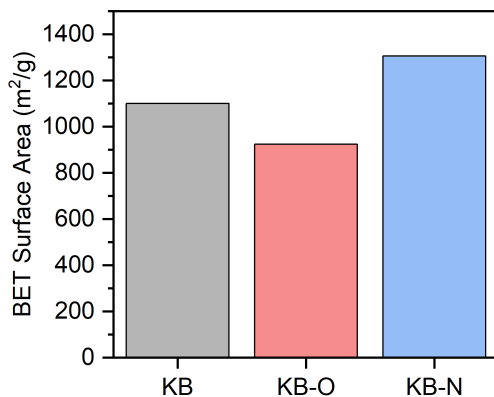
Figure 4.1: BET surface areas of KB, KB-O, and KB-N measured by N_2 adsorption

4.1.2 X-ray Photoelectron Spectroscopy

Figure 4.2 shows the XPS survey measurements and N 1s spectra for KB, KB-O, and KB-N. All three carbon powders exhibit clear peaks at the binding energies corresponding to C 1s (284-285 eV) and O 1s (532-534 eV). The O 1s peak has the highest relative intensity for KB-O, confirming the addition of oxygen-containing surface groups on this sample. The survey measurements show no visible peak for the N 1s signal (around 400 eV), suggesting the N content is fairly low for all samples, including KB-N. However, the N 1s spectra become visible at higher resolution. KB-N has a visible peak between 397-404 eV with the highest intensity around 398-399 eV, which corresponds to the binding energies for pyridinic and pyrrolic N (usually assigned to around 398 and 400 eV, respectively [117]). This result has been observed for carbon black functionalized by ammonolysis at 400-800°C, which yields mostly pyridinic and pyrrolic N [118]. Based on experimental results, the authors of this study postulate that adding pyridinic N groups in the carbon support leads to a better ionomer distribution, and thus better PEM fuel cell performance [118].

Meanwhile, KB-O exhibits two peaks, with the stronger one (405-408 eV) corresponding to nitrogen oxides and the weaker one (398-403 eV) possibly corresponding to quaternary and pyrrolic N. These signals indicate residue from nitric acid treatment, and the results corroborate a previous study with carbon black oxidized using nitric acid [67]. KB does not show any visible peaks in its N 1s spectrum.
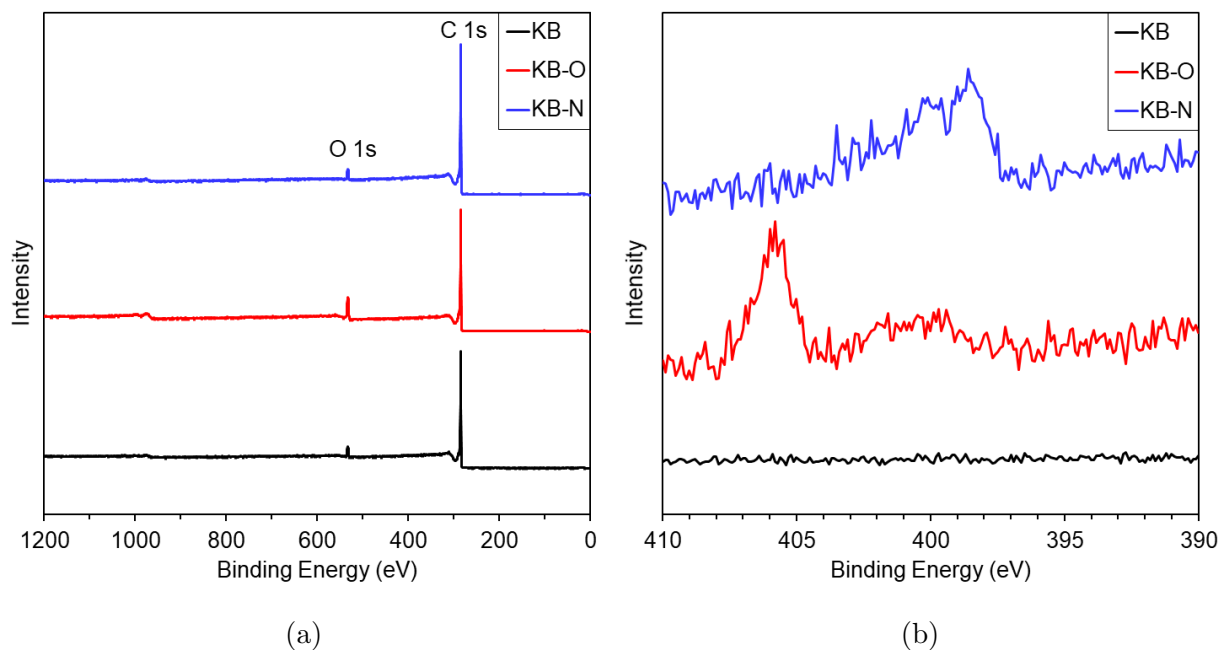

(a)   (b)

Figure 4.2: XPS spectra measured on KB, KB-O, and KB-N: a) Full scan, b) N 1s spectra

4.2   Pt/C Catalyst Properties

4.2.1   Transmission Electron Microscopy

Figures 4.3 (a, c, e) and 4.4 (a, c, e) show representative TEM images captured at 100kx and 200kx magnification, respectively, for the 3 small-scale catalyst samples. Images with 400kx magnification are also available in Figure A.3. Pt/KB is composed of small NPs (approx. 2 nm diameter) along with some larger NPs or agglomerates ($\geq$ 8 nm). In contrast, Pt/KB-O contains many medium-sized NPs (approx. 5 nm) and a few small NPs, and Pt/KB-N also has a mixture of small and medium-sized NPs. Amongst the medium-sized NPs, there appear to be some cube-like, elongated, and a few triangular shapes present, indicating limited shape-directed growth during the one-pot synthesis process. Figure A.4 shows the crystal lattice arrangements of the NPs, visible in high-resolution TEM images captured at 400kx magnification. These lattice arrangements indicate the crystallinity of the NPs. The atomic spacing is approximately 0.22-0.23 nm, consistent with other Pt(111)-dominated nanostructures reported in literature [82, 105]. This suggests that the polyhedral NPs exhibit octahedral, truncated octahedral, or possibly tetrahedral morphologies.

The differences in NP size and distribution can be explained by differences in the modified carbon's surface chemistry and microstructure. For example, the medium-sized NPs in Pt/KB-O and Pt/KB-N are dispersed slightly better than the large agglomerates in Pt/KB. This result highlights the function of newly introduced surface groups, namely oxygen-containing groups in KB-O and nitrogen groups in KB-N, as binding sites for Pt NPs. The binding sites allow both small and medium/large NPs to coexist in an evenly dispersed fashion. Furthermore, Pt/KB-O has a larger NP size than Pt/KB and Pt/KB-N, which can be explained by two reasons. First, KB-O has the lowest BET surface area out

of the three carbon supports, so fewer small NPs can nucleate on KB-O compared to KB and KB-N. Second, oxidizing acid treatment is known to make the carbon surface more electronegative. The Pt precursor used in this work contains negatively charged groups ($PtCl_6^{2-}$), so it would be more difficult for small Pt NPs to nucleate on KB-O compared to KB and KB-N. Overall, the TEM images suggest that surface groups on both KB-O and KB-N improve the dispersion of NPs on the support, which should theoretically benefit the catalyst because of increased ECSA.

Figures 4.3 (b, d, f) and 4.4 (b, d, f) show representative TEM images captured at 100kx and 200kx magnification, respectively, for the 3 large-scale catalyst samples. Images with 50kx and 400kx magnification are also available in Figure A.1 and A.3, respectively. Pt/KB-10x is noticeably different from Pt/KB, with some of its NPs being replaced by short nanowire- or nanorod-like structures. Meanwhile, Pt/KB-O-10x and Pt/KB-N-10x are visually more similar to their small-scale versions; both are characterized by a mixture of small- and medium-sized NPs (although Pt/KB-O-10x also contains some nanorods, as shown in Figure A.2). As before, Pt/KB-O-10x contains more medium-sized NPs and Pt/KB-N-10x more small NPs. The medium-sized and large NPs are dispersed more evenly with less agglomeration in Pt/KB-O-10x and Pt/KB-N-10x compared to Pt/KB-10x. As before, some of the NPs have non-spherical or polyhedron-like morphologies. Atomic spacing corresponding to Pt(111) is observed in both the NPs and nanorods.

Comparing the catalysts synthesized in small scale and large scale, it seems that the larger thermal and concentration gradients in the large-scale synthesis setup affect the catalyst differently depending on which carbon is used. For instance, the mean NP sizes generally increase after scaling up; this trend could be due to a lower average temperature in the larger flask used to synthesize the catalyst. However, the NP size increases the most

for Pt/KB-10x, whereas there is little to no increase for Pt/KB-O-10x and Pt/KB-N-10x. The latter two catalysts are also visually more similar to their small-scale versions compared to Pt/KB-10x, suggesting that functionalizing the carbon support may promote a more consistent or predictable catalyst morphology when the catalyst synthesis is scaled up. Another new observation is that Pt/KB-10x contains the most nanorod-like shapes. The formation of nanorods serves as evidence of shape-controlling agents generated in the alkaline EG+DMF system, as such an anisotropic growth pattern would be thermodynamically unfavorable in the absence of shape-controlling species. Larger thermal and concentration gradients in the large flask may create favorable conditions for nanowire/nanorod growth in isolated locations during the reaction. Further refinements to the reaction conditions and choice of carbon support could help control the formation of NPs vs. nanorods using this synthesis method. Meanwhile, nanorod formation is inhibited for Pt/KB-O-10x and Pt/KB-N-10x because KB-O and KB-N contain more binding sites for individual NPs, so they remain visually similar to the small-scale versions.

(a) Pt/KB

(b) Pt/KB-10x

(c) Pt/KB-O

(d) Pt/KB-O-10x
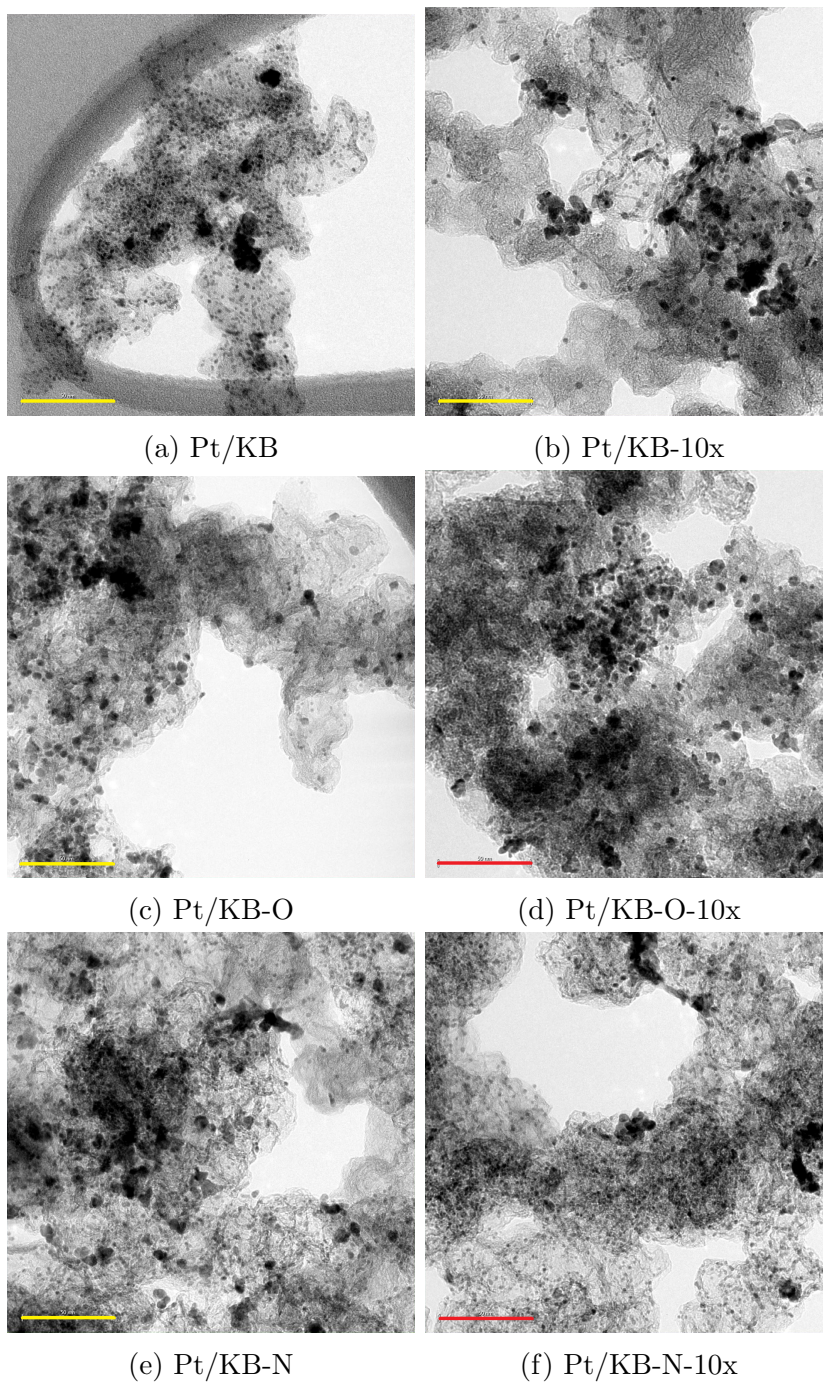
(e) Pt/KB-N

(f) Pt/KB-N-10x

Figure 4.3: TEM images of all catalysts captured at 100kx magnification (scale bars are 50 nm)

(a) Pt/KB

(b) Pt/KB-10x

(c) Pt/KB-O

(d) Pt/KB-O-10x
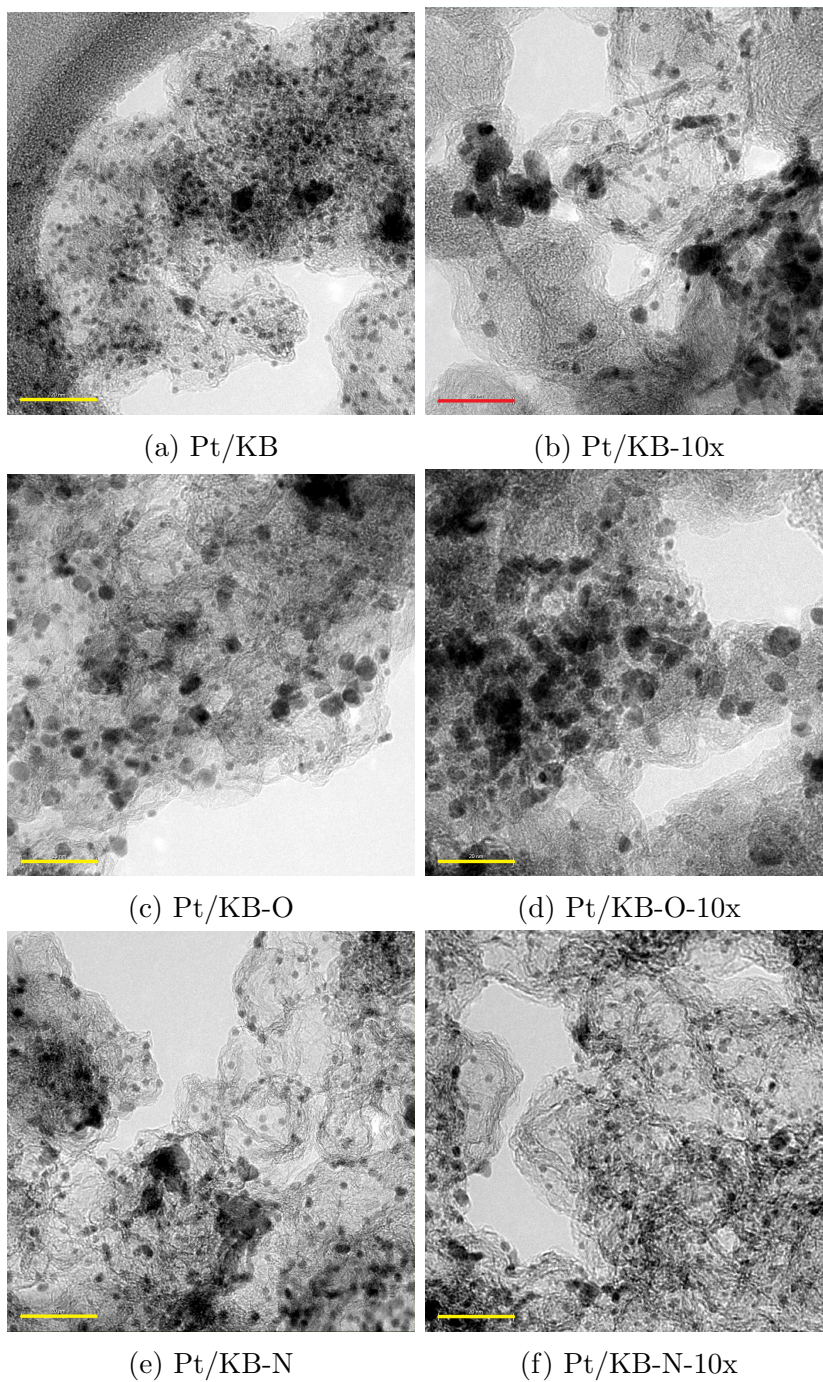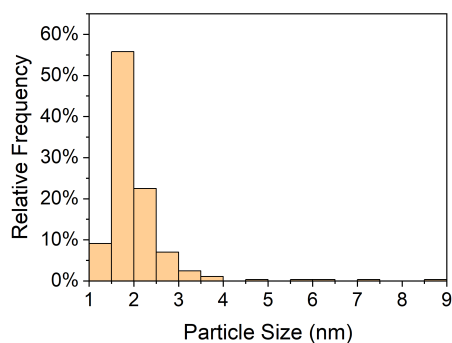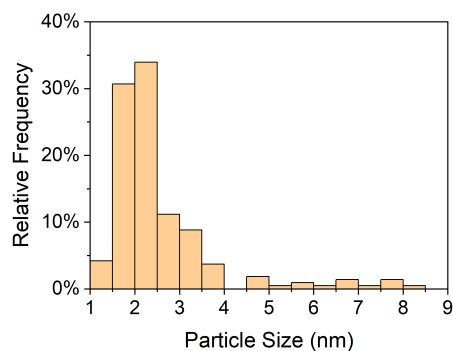
(e) Pt/KB-N

(f) Pt/KB-N-10x

Figure 4.4: TEM images of all catalysts captured at 200kx magnification (scale bars are 20 nm)

Figure 4.5 shows the histograms estimating the particle size distributions for all 6 catalysts based on the 200kx magnification images. From this data, the mean NP sizes for Pt/KB, Pt/KB-O, and Pt/KB-N are 2.1, 3.2, and 2.4 nm, respectively. As expected from the images, the majority of NPs in Pt/KB and Pt/KB-N are close to 2 nm in diameter, and only a handful are larger than this. However, there would be a disproportionate amount of Pt atoms inside the few large NPs because the volume of the NPs scales with the size cubed. Thus, there is still much potential to improve the catalyst dispersion and relocate the Pt atoms into smaller NPs. For Pt/KB-O, most of the NPs are between 2-5 nm in diameter, demonstrating the successful nucleation of both small and medium-sized NPs. However, the wide variance in particle size indicates that the synthesis procedure can be improved further to achieve a more uniform size distribution. For the large-scale samples, the NP sizes for Pt/KB-10x, Pt/KB-O-10x, and Pt/KB-N-10x are 2.6, 3.5, and 2.4 nm, respectively. The overall increase in size for Pt/KB-10x and Pt/KB-O-10x is due to a loss of very small NPs.

The variation of sizes in all 6 samples suggests that further optimization of the alkaline EG+DMF synthesis method is needed to produce regularly sized Pt NPs. In a separate experiment (Appendix B), this synthesis method did successfully yield well-dispersed and more regularly sized polyhedral NPs on non-functionalized carbon. The batch of catalyst contained a lower Pt content (32 wt.%) and used a slightly different procedure (reagent amounts, methods of mixing/dispersing the Pt precursor and carbon). Thus, when used as a one-pot synthesis method, the alkaline EG+DMF method is sensitive to many different parameters. Further experimentation using small catalyst batches could help optimize such parameters to produce more regular non-spherical NPs.
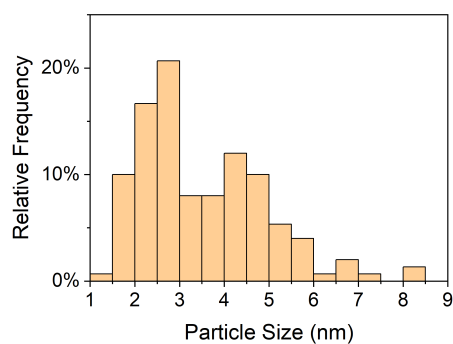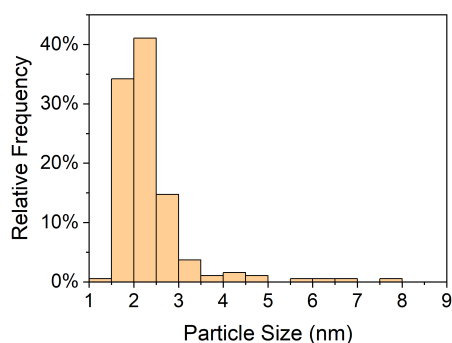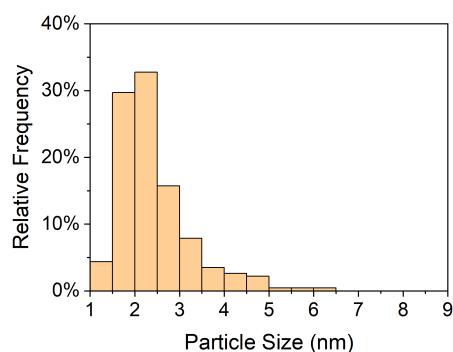
(a) Pt/KB

(b) Pt/KB-10x
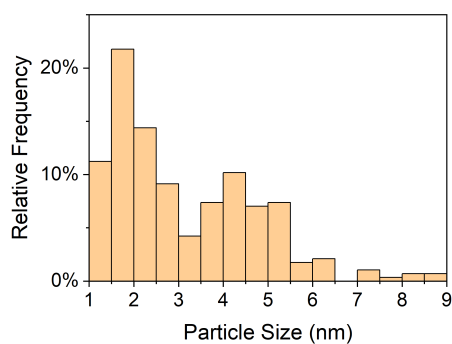
(c) Pt/KB-O

(d) Pt/KB-O-10x

(e) Pt/KB-N

(f) Pt/KB-N-10x

Figure 4.5: Particle size distributions for all catalysts; note that the size distributions for large-scale samples exclude the nanorods

4.2.2   X-ray Diffraction

Figure 4.6 shows the XRD pattern of Pt/KB-10x, Pt/KB-O-10x, and Pt/KB-N-10x. All the samples display clear peaks corresponding to Pt(111), Pt(200), Pt(220), Pt(311), and Pt(222), confirming the crystalline structure of the Pt catalyst. The peak locations and relative intensities are similar to those measured on commercial Pt/C catalysts [29]. The ratio between Pt(200) and Pt(111) intensity for Pt/KB-10x, Pt/KB-O-10x, and Pt/KB-N-10x is approximately 39:100, 40:100, and 34:100, respectively. Since the standard face-centered-cubic Pt pattern has been suggested to exhibit a ratio of 52:100 [92], all three catalysts seem to be polyhedral or slightly Pt(111)-dominated, with Pt/KB-N-10x being the most Pt(111)-dominated. This supports the high-resolution TEM images showing atomic spacing corresponding to Pt(111). In addition, the Pt(111) peak of each sample is scanned at a slower rate to measure peak broadening, based on which the crystallite size is estimated to be 5.8, 5.6, and 5.6 nm, respectively. These values are noticeably larger than the mean sizes determined from TEM. A plausible explanation is that the samples contain many small NPs, which result in a small mean size according to TEM, but the small NPs also have very small volume so their large quantity does not accurately represent the actual distribution of Pt atoms. In reality, many Pt atoms are located within the few large NPs and agglomerates, which is probably what is being captured by the XRD results. Therefore, the mean particle size from TEM and mean crystallite size from XRD may not match for samples with uneven particle size distributions, such as the catalysts in this work.
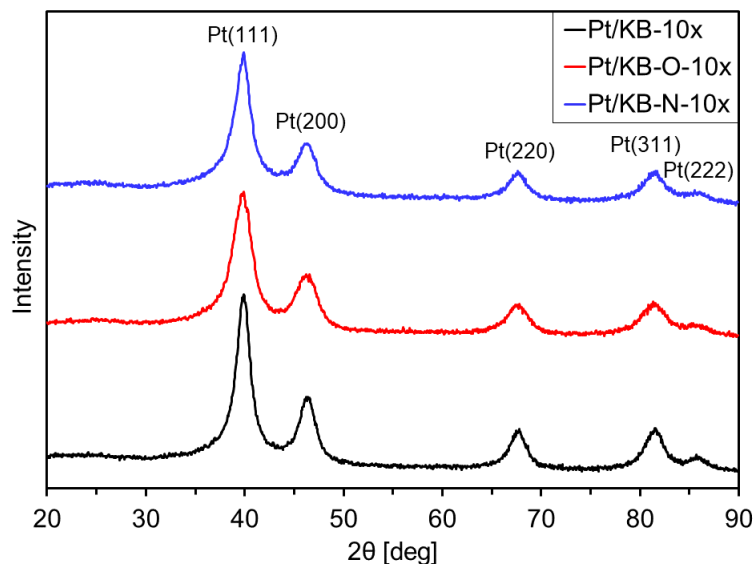
Figure 4.6: XRD patterns for Pt/KB-10x, Pt/KB-O-10x, and Pt/KB-N-10x

4.2.3 Thermogravimetric Analysis

From TGA measurement, the Pt loadings for Pt/KB, Pt/KB-O, and Pt/KB-N are all estimated to be between 48-52%, close to the nominal Pt loading of 48.5%. This confirms most of the Pt precursor is successfully reduced and deposited onto the carbon support. Even when the synthesis procedure is repeated several times for the small-scale samples (to check consistency), all the batches achieve Pt loadings within this range. Meanwhile, the Pt content in the large-scale batches of Pt/KB-10x, Pt/KB-O-10x, and Pt/KB-N-10x is approximately 47, 49, and 43 wt.%, respectively. Pt/KB-10x and Pt/KB-O-10x are near the nominal value of 48.5 wt.%, confirming that using larger batches does not negatively impact the extent of Pt precursor reduction when synthesizing these samples. However, the Pt content in Pt/KB-N-10x is noticeably lower, which is unexpected given that Pt/KB-N has near-nominal Pt content. This anomaly may have been caused by experimental

61

factors, for example, water trapped inside the carbon micropores not being fully removed during the TGA measurement. Regardless, the fact that all the catalyst have similar Pt loadings (43-52 wt.%) demonstrates that their morphological differences are due to the carbon support properties and not Pt loading.

Figure 4.7 shows TGA graphs for the large-scale samples. The mass decrease from carbon oxidation occurs at different temperatures, with Pt/KB-O-10x losing mass at the lowest temperature and Pt/KB-N-10x at the highest temperature, despite all catalysts having similar Pt loadings. A similar trend is observed for the small-scale samples. This observation shows that KB-O is less thermally stable and KB-N more thermally stable than KB. Additionally, the steep drops around 150-175°C for Pt/KB-10x and Pt/KB-O-10x might indicate the presence of surfactants that were not successfully removed during the catalyst washing/collection process. This may be problematic if the catalysts are used in PEM fuel cells without further treatment, and more effective surfactant removal techniques may need to be investigated. Regardless, the performance of all catalysts is observed to stabilize after sufficient voltage cycling (done before all CV measurements), so this is not an issue for the present work.

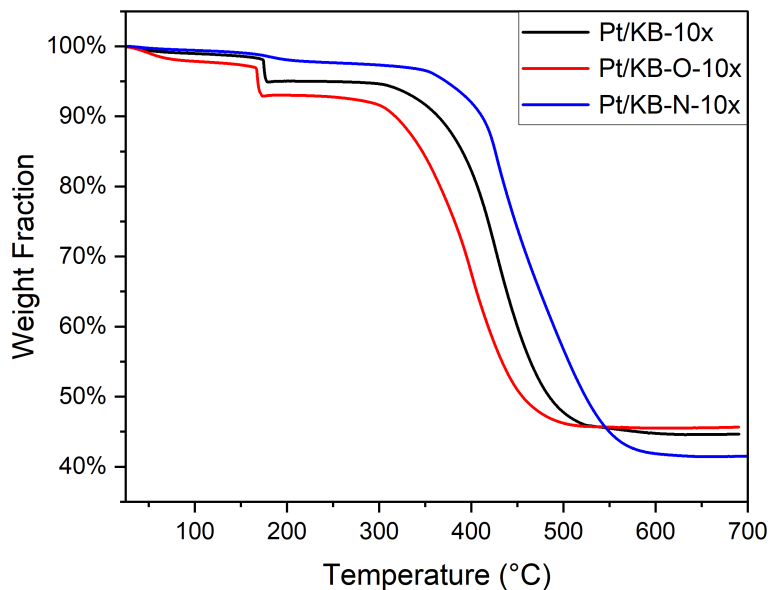Figure 4.7: TGA curves for Pt/KB-10x, Pt/KB-O-10x, and Pt/KB-N-10x

4.2.4 Summary

Physical characterization tests confirm the impacts of both oxygen and nitrogen functional-ization on the properties of carbon and carbon-supported Pt catalyst. In particular, there are noticeable changes in the carbon's surface chemistry and textural properties (BET area), and the catalysts' NP size distributions and morphologies differ from each other despite having been synthesized using the same method. The TEM images also reveal qualitative insights such as the improved NP dispersion and consistency upon scale-up for the catalysts on functionalized carbon black. These changes can be used to explain any differences in electrochemical and fuel cell performance of the catalysts.

Table 4.1: Summary of physical characterization test results

| Catalyst	Carbon BET Area [m^2/g]	NP Size (TEM) [nm]	(XRD) [nm]	Pt Loading [wt.%]
Pt/KB	1101	2.1		50
Pt/KB-O	924	3.2		51
Pt/KB-N	1305	2.4		50
Pt/KB-10x	1101	2.6	5.8	47
Pt/KB-O-10x	924	3.5	5.6	49
Pt/KB-N-10x	1305	2.4	5.6	43

4.3 Electrochemical Performance

4.3.1 Catalyst Activity

Figure 4.8a compares the average CV curves obtained for Pt/KB, Pt/KB-O, and Pt/KB-N. Based on the hydrogen desorption peak area (measured using the baseline at 0.4 V), the ECSA for these catalysts is 25, 31, and 25 m^2/g, respectively. Figure 4.8c shows the ECSAs with error bars representing 95% confidence intervals, showing that Pt/KB-O has a higher ECSA than Pt/KB and Pt/KB-N by a significant margin. At first glance, the lower ECSAs of Pt/KB and Pt/KB-N seem to contradict their TEM images, which show large amounts of small NPs that should exhibit a higher area-to-volume ratio compared to Pt/KB-O. This could be explained by the large particles/agglomerates in the catalysts, which contain a substantial fraction of the Pt volume. In contrast, Pt/KB-O has enough of the catalyst in the form of medium-sized NPs (rather than the large particles/agglomerates) to produce a higher overall ECSA. Additionally, the middle part of the CV curve (approx. 0.4-0.6 V) for Pt/KB-O confirms the modified surface chemistry of KB-O. As explained in Chapter 2.2, the oxygen-containing surface groups enhance the carbon's hydrophilicity, increasing the

accessibility to the aqueous electrolyte and widening the double-layer capacitance region. Pt/KB-O also shows slight peaks near 0.55-0.6 V, consistent with the redox reaction of oxygen-containing groups as observed in previous studies [65].

Figure 4.8b compares the average CV curves obtained for Pt/KB-10x, Pt/KB-O-10x, and Pt/KB-N-10x on the same y-axis as Figure 4.8a. These catalysts have an ECSA of 24, 25, and 31 m^2/g, respectively. Compared to Pt/KB, Pt/KB-10x maintains a similar ECSA despite having fewer small NPs, perhaps because the nanorods' high surface area makes up for the loss of small NPs. Meanwhile, Pt/KB-O-10x loses ECSA significantly because it contains fewer nanorods to counter its loss of small NPs, and Pt/KB-N-10x achieves a relatively high ECSA because it preserves the large quantity of small NPs.
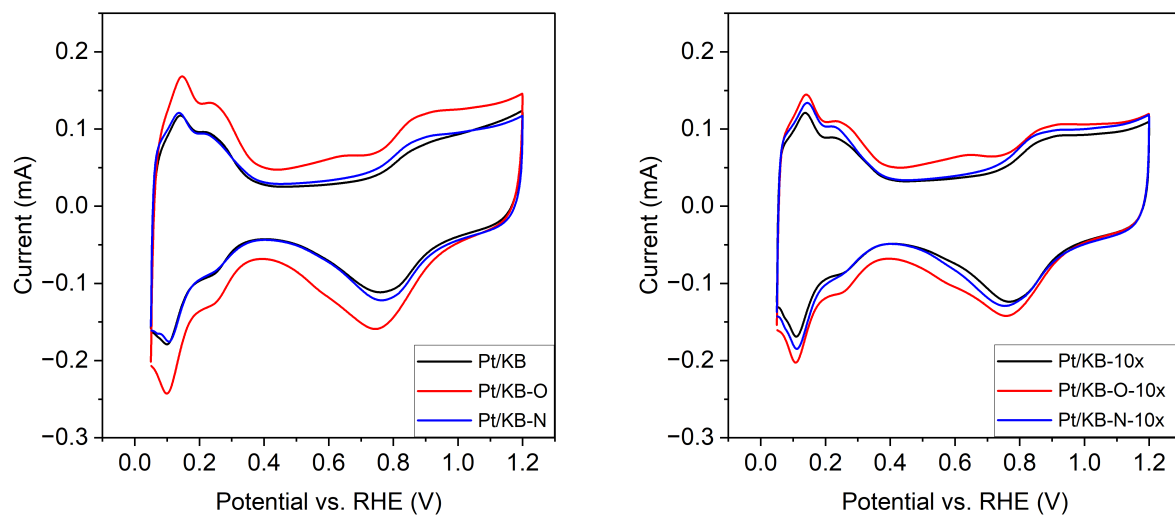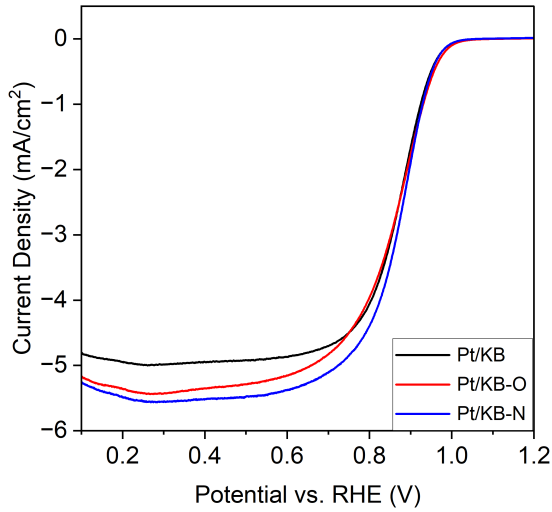
(a)

(b)
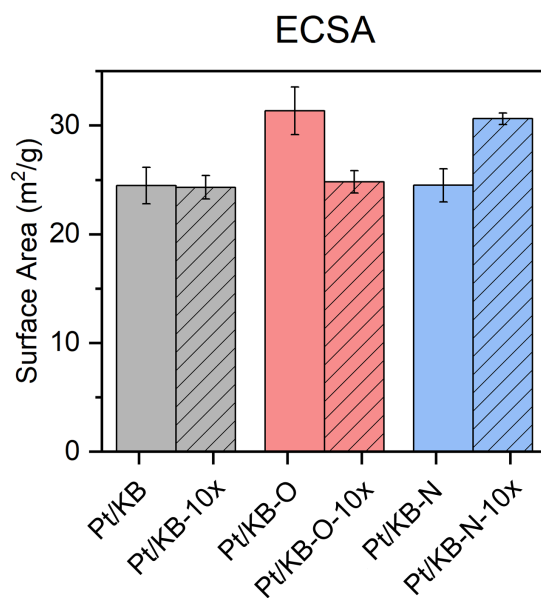
(c)

Figure 4.8: Cyclic voltammetry curves measured in 0.1 M HClO$_4$ electrolyte for: a) Pt/KB, Pt/KB-O, Pt/KB-N, and b) Pt/KB-10x, Pt/KB-O-10x, Pt/KB-N-10x; c) Comparison of ECSA with 95% confidence intervals

Figure 4.9a compares the average LSV curves for Pt/KB, Pt/KB-O, and Pt/KB-N. The MA towards the ORR at 0.9 V (vs. RHE) for these catalysts is 101, 103, and 115 A/g, respectively. Combined with the ECSA measurements corresponding to the LSV tests, the SA is 4.1, 3.2, and 4.7 A/m^2, respectively. These values are compared graphically with 95% confidence intervals in Figures 4.9c and 4.9d. The half-wave potential ($E_{1/2}$) calculated based on the limiting current at 0.3 V is 872, 864, and 874 mV, respectively. Pt/KB-O achieves similar or slightly lower ORR activity as Pt/KB, and Pt/KB-N achieves similar or slightly higher activity. Given that Pt/KB-N has similar ECSA as Pt/KB, the minor improvement can be attributed to the properties of KB-N, which foster a slightly more uniform NP distribution and possibly more optimal electronic interaction between the catalyst and support.

The result for Pt/KB-O is notable because its MA is only similar to Pt/KB despite having a higher ECSA, and it shows the least steep LSV curve (reflecting the lowest $E_{1/2}$). A possible explanation is ionomer poisoning on the Pt catalyst surface, which is known to decrease ORR activity. Since Pt/KB-O has larger mean NP size and KB-O has lower BET surface area, the NPs are more likely to be on the carbon surface and not inside the small micropores, so they are more susceptible to ionomer adsorption. The sulfonic anion adsorption on Pt results in a local O$_2$ transport resistance, lowering the current density magnitude of Pt/KB-O in the diffusion-influenced region (around 0.3-0.8 V) despite showing similar kinetic activity (above 0.9 V) as the other catalysts. This hypothesis is supported by a previous study, which found that Pt NPs on the surface are more sensitive to Nafion loading in terms of its effect on ORR activity [119]. Furthermore, the KB-O surface is expected to be negatively charged relative to untreated carbon, so the ionomer's negatively charged sulfonate groups might preferentially adsorb onto Pt instead of carbon. Therefore, functionalizing the carbon support with oxidizing acids does not necessarily

improve the catalyst's activity as the increased ionomer adsorption on Pt may reduce its SA, offsetting the benefit from its high ECSA. This phenomenon may also contribute to the slightly higher performance of Pt/KB-N, enabled by the high BET area of KB-N and abundance of small NPs in the catalyst. It is plausible that much of the catalyst in Pt/KB-N is located in micropores and thus protected from ionomer poisoning.

Figure 4.9b compares the average LSV curves for Pt/KB-10x, Pt/KB-O-10x, and Pt/KB-N-10x. The MA towards the ORR of these catalysts is 141, 114, and 148 A/g, respectively, corresponding to SA of 5.7, 4.7, and 4.9 A/m^2, respectively. The $E_{1/2}$ is 881, 873, and 880 mV, respectively, consistent with the trends in MA and SA. Unexpectedly, all three catalysts become more active upon scale-up. Pt/KB-10x shows a significant improvement compared to Pt/KB and even achieves the highest SA of all catalyst samples in this work. A possible explanation is the abundance of Pt(111)-oriented nanorods, whose unconventional morphology results in high inherent ORR activity even in the absence of benefits from carbon support functionalization. Pt/KB-O-10x shows a significant increase in SA compared to Pt/KB-O, but its activity is still lower than that of Pt/KB-10x, as it contains fewer nanorods and may be subject to the same ionomer poisoning effect as Pt/KB-O. Finally, Pt/KB-N-10x seems to increase in MA compared to Pt/KB-N because of its higher ECSA, though experimental variability makes it difficult to confirm whether the change is significant. However, the SA of Pt/KB-N-10x remains almost the same as Pt/KB-N, which reflects the similar mean NP size and morphology of these two samples (larger NPs are known to exhibit higher SA [88]). These results show that carbon support functionalization does not always improve non-spherical catalysts, as the effect of functionalization on catalyst size and morphology (e.g., nanorods) can lead to unpredictable differences in the ORR activity.
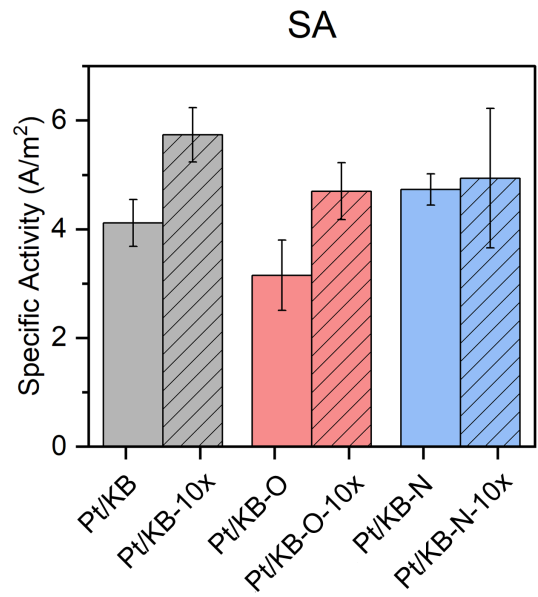
(a)
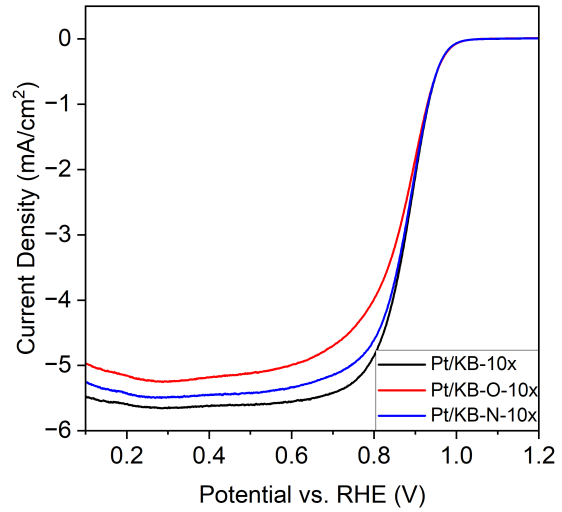
(b)
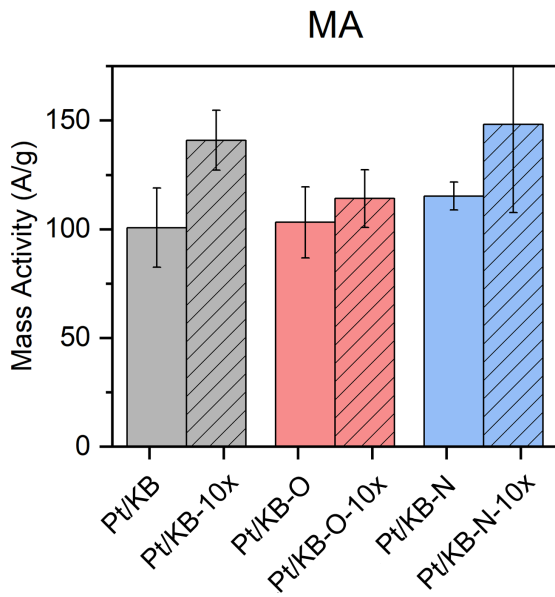
(c)

(d)

Figure 4.9: Linear sweep voltammetry curves measured in 0.1 M HClO$_4$ electrolyte for: a) Pt/KB, Pt/KB-O, Pt/KB-N, and b) Pt/KB-10x, Pt/KB-O-10x, Pt/KB-N-10x; Comparison of c) MA and d) SA with 95% confidence intervals

69

4.3.2 Catalyst Durability

Figure 4.10 summarizes the changes in ECSA during the catalyst AST between 0.5-1 V (vs. RHE), and Figure 4.11 shows the corresponding CV curves before and after the test. Pt/KB loses approximately 17% of its initial ECSA after 20,000 potential cycles, whereas Pt/KB-O and Pt/KB-N lose 23% and 24%, respectively. All 3 of the large-scale samples lose 22-24% of their initial ECSA. Based on these results, substituting KB with KB-O or KB-N does not necessarily increase the durability of the supported Pt catalyst, and may in fact decrease it. An AST like this one is expected to degrade the catalyst via Ostwald ripening (wherein Pt atoms detach from smaller NPs and re-deposit onto larger NPs) or particle coalescence, both of which increase the average NP size and decrease ECSA [23, 120]. For catalysts supported on Ketjen Black, a porous high-surface-area carbon support, the electrochemical degradation is thought to be dominated by Ostwald ripening [23]. Therefore, it is reasonable to conclude that the functional groups do little to prevent the Pt NPs from degrading via Ostwald ripening. To support this, the segment between the H_2 desorption region and Pt oxidation region (around 0.4-0.6 V) is mostly unchanged by the test, indicating that the carbon support is unaffected and the test primarily degrades the metal catalyst. Thus, carbon corrosion can be ruled out as a cause of catalyst degradation in this AST.
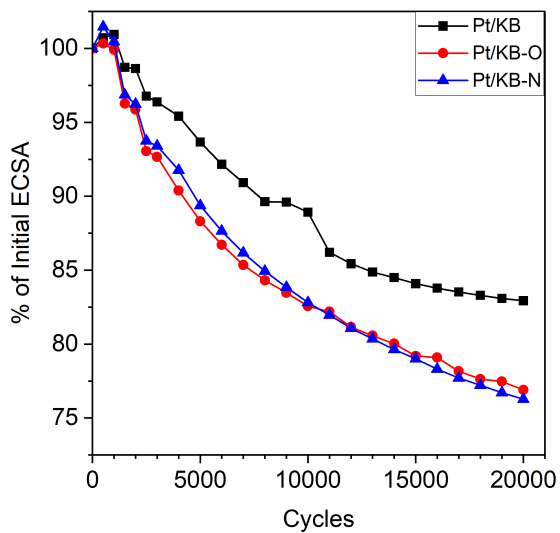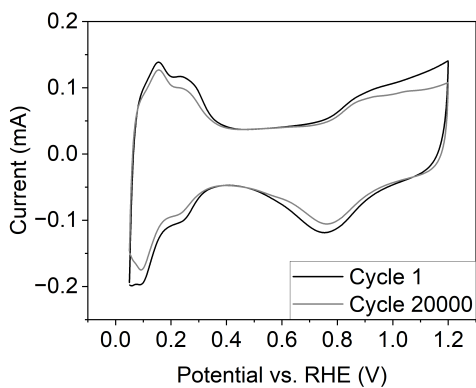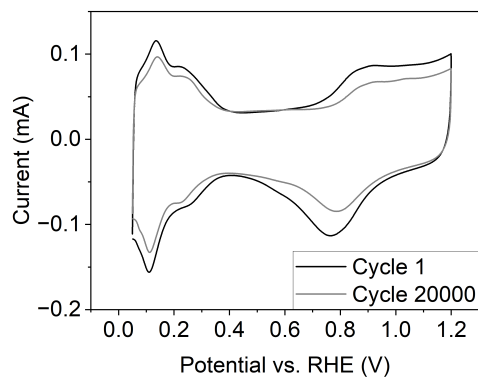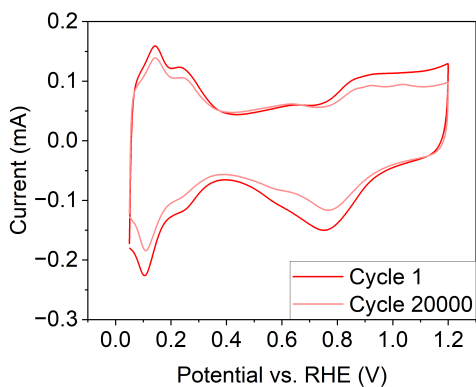
(a)
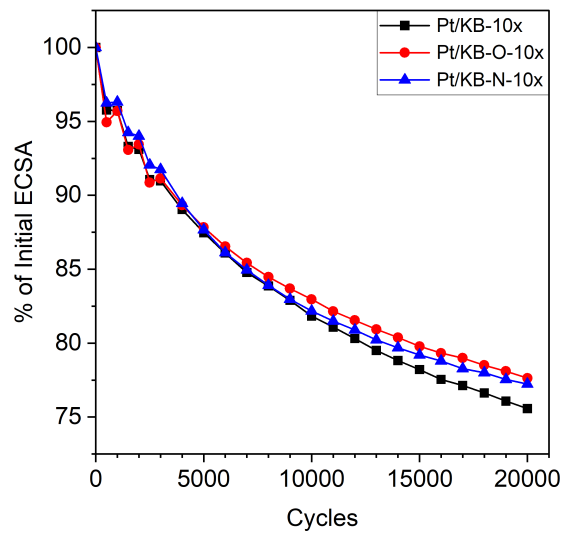
(b)

Figure 4.10: Comparison of ECSA degradation rates during the catalyst AST for: a) Pt/KB, Pt/KB-O, Pt/KB-N, and b) Pt/KB-10x, Pt/KB-O-10x, Pt/KB-N-10x
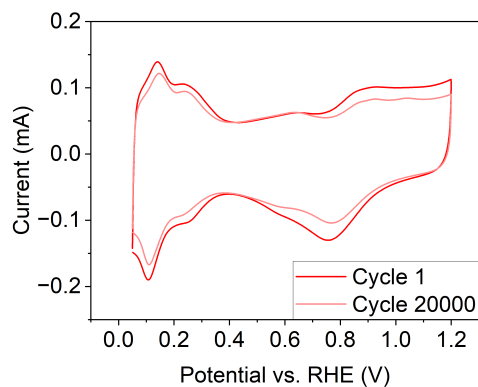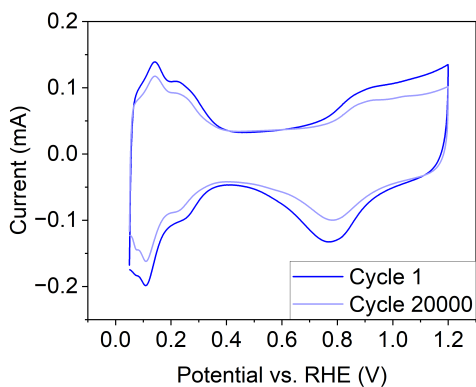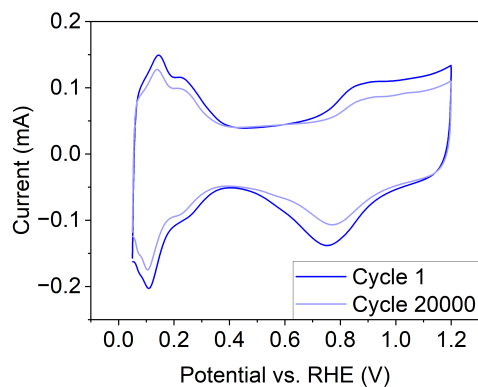
(a) Pt/KB

(b) Pt/KB-10x

(c) Pt/KB-O

(d) Pt/KB-O-10x

(e) Pt/KB-N

(f) Pt/KB-N-10x

Figure 4.11: CV measurements before and after the catalyst AST for all catalysts

Figure 4.12 summarizes the changes in ECSA during the corrosion AST between 1-1.5 V (vs. RHE), and Figure 4.13 shows the corresponding CV curves before and after the test. In this test, Pt/KB, Pt/KB-O, and Pt/KB-N lose 18%, 4%, and 12%, respectively, of their initial ECSA after 5,000 cycles. The large-scale catalysts show a similar trend, with Pt/KB-10x, Pt/KB-O-10x, and Pt/KB-N-10x losing 17%, 7%, and 21%, respectively. The Pt catalysts on KB-O are most resistant against ECSA loss, which may be a surprising result as this functionalization method is expected to make the carbon more prone to corrosion [65]. There are a few possible explanations for this seemingly anomalous result. First, unlike the catalyst AST, the corrosion AST is expected to cause Pt particle detachment in addition to some agglomeration [120, 121]. Since Pt/KB-O and Pt/KB-O-10x have fewer small NPs (which are more thermodynamically unstable) than the other catalysts, they may be more resistant to Pt detachment. This resistance may be bolstered by the strong adhesion between Pt and surface oxygen groups [66]. Second, KB and KB-N seem to gain more new oxygen-containing groups (carboxyl, carbonyl, etc.), signaling the corrosion and poisoning of the Pt catalyst [121]. The formation of these groups is confirmed by the widening and slight peaks in the 0.4-0.6 V region of the cyclic voltammograms [65]. From Figure 4.13, these changes are most prominent for KB and KB-N, whereas KB-O only changes slightly (possibly because the existing groups formed during the oxidation treatment protect the surface from further corrosion).

The corrosion AST shows that carbon functionalization may indirectly affect the durability of Pt catalyst in high-voltage or corrosive conditions by limiting the effects of particle detachment or newly formed oxygen-containing groups. However, this discussion is speculative and cannot determine which degradation mechanism is most responsible for the ECSA loss. More detailed studies with techniques such as identical-location TEM imaging [120] would clarify the impact of oxidation-treated carbon on Pt catalyst durability.

Repeating the test with catalysts on nitrogen-doped carbon would also be worthwhile, as some studies have found that dopants can improve the catalyst's stability, whereas this was not realized in the present work.

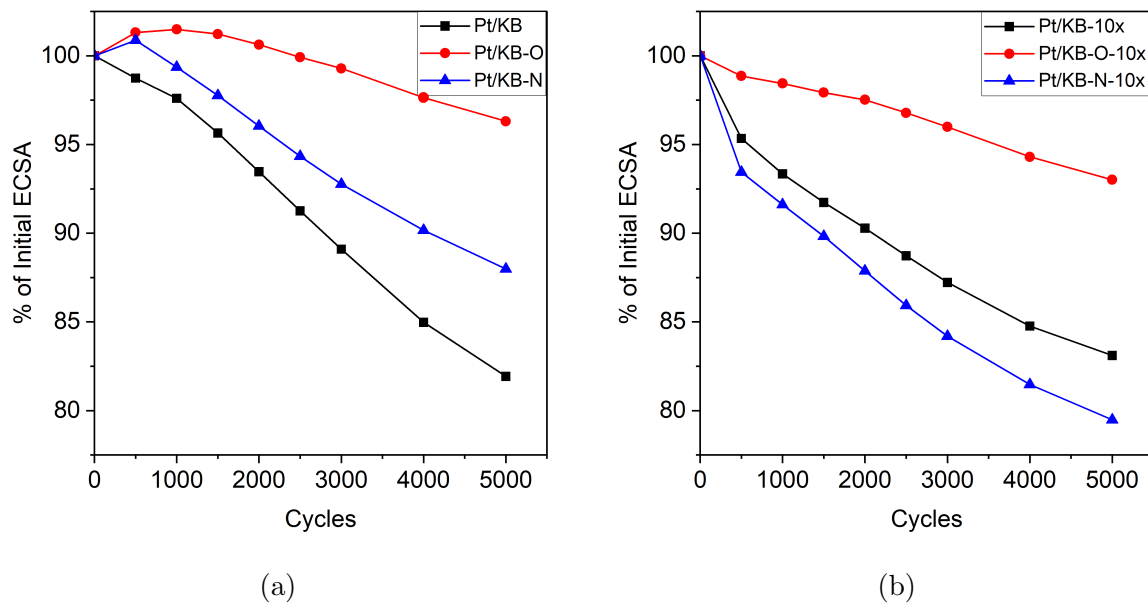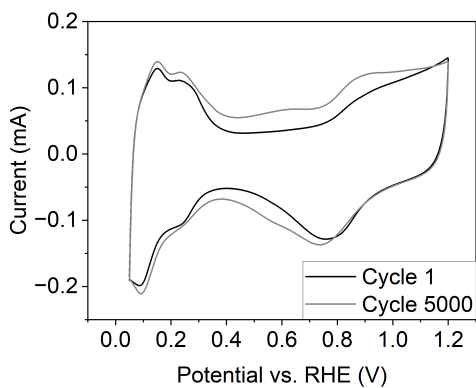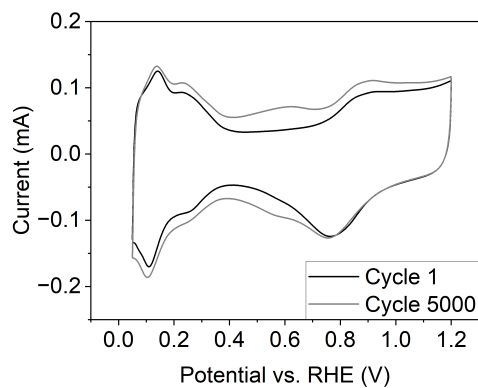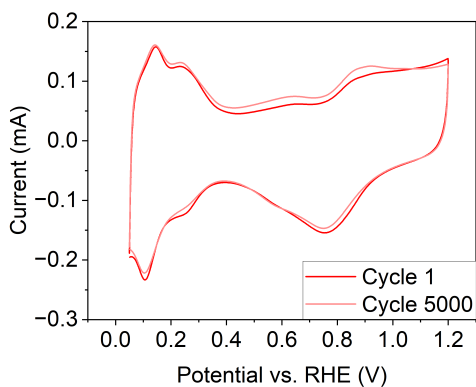(a)   (b)

Figure 4.12: Comparison of ECSA degradation rates during the carbon corrosion AST for: a) Pt/KB, Pt/KB-O, Pt/KB-N, and b) Pt/KB-10x, Pt/KB-O-10x, Pt/KB-N-10x
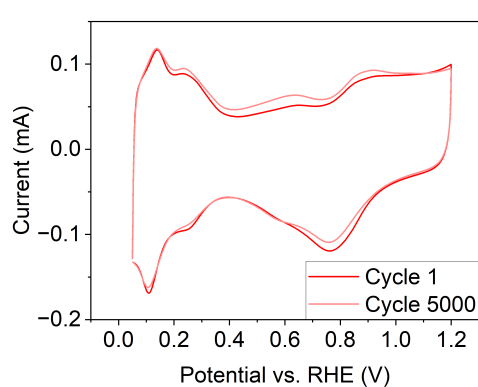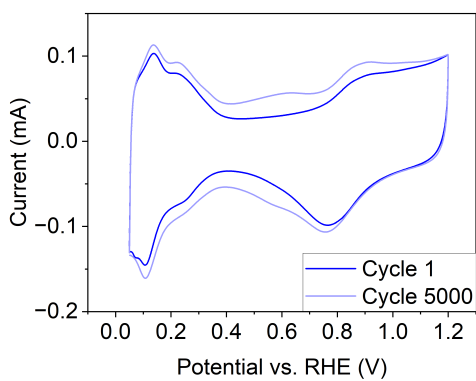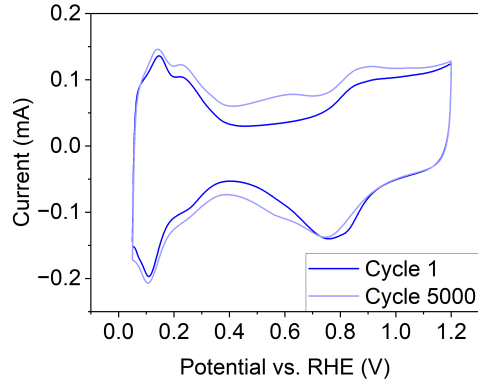
(a) Pt/KB

(b) Pt/KB-10x

(c) Pt/KB-O

(d) Pt/KB-O-10x

(e) Pt/KB-N

(f) Pt/KB-N-10x

Figure 4.13: CV measurements before and after the corrosion AST for all catalysts

4.3.3 Implications for Single-Cell Performance

Although the half-cell test results enable a detailed study of how different carbon varieties affect ORR activity and durability of Pt catalyst, these results do not always carry over to single-cell testing [29]. Nevertheless, other studies indicate that functionalizing the carbon support may enhance the performance of MEAs. For example, a study found that functionalizing multi-walled CNT support with oxidizing acids increases the MEA peak power density, with possible reasons being good Pt particle dispersion and the support's higher hydrophilicity (which may enhance water management) [24]. This result indicates that the improved Pt NP dispersion observed for Pt/KB-O and Pt/KB-N in the present work could possibly enable better MEA performance. The effect of hydrophilicity on MEA performance is more difficult to deduce because water management in PEM fuel cells depends on a multitude of other factors such as operating conditions and unit cell design. Furthermore, the modified microporous structure of KB-O (as suggested by its reduced BET area) may affect MEA performance, as the pore size distribution is known to affect mass transport of oxygen and water in the cathode [115]. These complexities show how the carbon's surface chemistry and microstructure can influence water management, and hence mass transport polarization, in an actual MEA.

Likewise, doping the carbon support with heteroatoms can improve certain characteristics of the Pt/C catalyst, but there is currently insufficient data on how it affects MEA performance and durability. A recent study found that N-doping the carbon leads to higher beginning-of-life performance of the Pt/C catalyst in an MEA, presumably because the N groups result in a better-distributed ionomer film [118]. The carbon leading to the best performance in that study had a high fraction of pyridinic N groups, likely similar to KB-N in this work. Therefore, if the authors' hypothesis is true, then Pt/KB-N could perform

76

substantially better than Pt/KB in MEA tests, where the influence of ionomer would be more important compared to in RDE tests. The authors also failed to achieve improved fuel cell durability against high-potential cycles (1-1.5 V) despite their previous physical test results showing better corrosion resistance of the N-doped carbon [67]. This discrepancy is similar to the current work, where the TGA results show better thermal stability for KB-N, yet there is no clear durability improvement in the corrosion AST for Pt/KB-N. However, a different study using an N-doped graphene and carbon black hybrid support observed better MEA durability in both kinds of ASTs (0.5-1 V and 1-1.5 V), which the authors attribute to the N groups' anchoring properties and stability against corrosion [60]. The authors' choice of a graphene + carbon black hybrid support may have changed the impact of N-doping compared to a pure carbon black support. Furthermore, non-spherical catalyst morphologies such as nanowires show good durability against potential cycling when combined with the anchoring properties of dopants [52]. More experimental data is needed to clarify the impact of N-doping on catalyst durability, and whether the corrosion resistance of the carbon itself correlates with that of the Pt/C catalyst.

4.3.4   Summary

Based on electrochemical tests, carbon functionalization generally has minor impacts on the Pt catalyst's activity or durability. Pt/KB-O achieves similar or slightly worse ORR activity than Pt/KB, but it demonstrates the best ECSA retention in the corrosion AST. Meanwhile, Pt/KB-N achieves similar or slightly better ORR activity than Pt/KB, along with similar durability. All the catalysts show improved ORR activity when the synthesis is scaled up, with Pt/KB-10x achieving the highest SA and $E_{1/2}$ out of all the catalysts in this study. A possible explanation is that the Pt nanorods unintentionally formed during

large-scale synthesis have high surface area and inherent activity. From these results, it remains inconclusive which functionalized carbon is best for fuel cell applications. Their performances could differ in MEA testing, where factors such as heat/water management, gaseous O_2 transport, and ionomer poisoning become important.

Table 4.2: Summary of electrochemical test results

Catalyst	ECSA $[m^2/g]$	MA $[A/g]$	SA $[A/m^2]$	$E_{1/2}$ $[mV]$	Catalyst AST (ECSA loss)	Corrosion AST (ECSA loss)
Pt/KB	25	101	4.1	872	17%	18%
Pt/KB-O	31	103	3.2	864	23%	4%
Pt/KB-N	25	115	4.7	874	24%	12%
Pt/KB-10x	24	141	5.7	881	24%	17%
Pt/KB-O-10x	25	114	4.7	873	22%	7%
Pt/KB-N-10x	31	148	4.9	880	22%	21%

Chapter 5

Conclusions and Recommendations

5.1   Conclusions

In this thesis work, non-spherical Pt catalyst samples are synthesized on differently func-
tionalized Ketjen Black carbons (KB), and the catalysts are evaluated using physical and
electrochemical testing. A one-pot surfactant-free synthesis method is chosen to empha-
size the importance of simple and scalable catalyst production for practical application in
proton exchange membrane (PEM) fuel cells.

Physical characterization on both the standalone carbons and carbon-supported Pt cat-
alysts generally supports results from previous studies. Functionalizing KB with oxidizing
acids (KB-O) introduces oxygen groups into the carbon surface, decreases its BET surface
area, and decreases its thermal stability. Meanwhile, applying a nitrogen-doping process
(KB-N) adds nitrogen surface groups, increases its surface area, and increases its thermal
stability. The changes to the carbon's surface chemistry and microstructure impact the size

and morphology of the non-spherical Pt catalyst when using a one-pot synthesis method. Pt/KB is composed of small nanoparticles (NPs) (around 2 nm) with a few medium-sized or large NPs and agglomerates ($\geq$ 5 nm), whereas Pt/KB-O and Pt/KB-N are dominated by well-dispersed NPs. The reduced BET area and modified surface chemistry of KB-O lead to a larger mean NP size. When the catalyst synthesis is repeated in 10x larger batches, Pt/KB-10x changes noticeably with most of the small NPs being replaced by nanorod-like structures, whereas Pt/KB-O-10x and Pt/KB-N-10x are visually similar to their small-scale counterparts. All the catalyst samples have similar Pt loadings between 43-52 wt.%, so these morphological differences can be attributed wholly to the carbon support properties. Overall, the results suggest that surface groups added by both functionalization methods can lead to better NP dispersion and more predictable morphology upon scale-up.

The differences in carbon properties and catalyst morphology affect the oxygen reduction reaction (ORR) activity and durability against potential cycling. From electrochemical tests, Pt/KB-O is found to have lower activity than Pt/KB and Pt/KB-N despite having higher electrochemically active surface area (ECSA); this result is consistent with poisoning from the sulfonate-based Nafion ionomer, which is expected to impact Pt/KB-O the most. Meanwhile, Pt/KB-N achieves similar or slightly higher activity compared to Pt/KB. All three catalysts achieve better ORR activity when the synthesis is scaled up, with Pt/KB-10x achieving the highest activity of 5.7 A/m^2. This improvement could originate from the Pt(111)-oriented nanorods with high surface area and activity, which were unintentionally formed with greatest yield in Pt/KB-10x. In the catalyst accelerated stress test (AST) between 0.5-1 V, neither Pt/KB-O nor Pt/KB-N is more durable than Pt/KB, revealing that the functional groups do little to prevent ECSA degradation via Ostwald ripening. However, in the corrosion AST between 1-1.5 V, Pt/KB-O retains more ECSA and undergoes

80

a lesser change in the carbon support compared to Pt/KB and Pt/KB-N. These results are attributed to a combination of a higher fraction of larger NPs, which may be more thermodynamically stable, and the fact that KB-O already has surface groups from the oxidizing acid functionalization, resulting in a passivation effect that prevents carbon corrosion during the AST. Therefore, the impact of carbon functionalization on non-spherical Pt catalyst is difficult to predict because of the complex differences in carbon properties and catalyst morphology. Nevertheless, it is useful to recognize how the different characteristics of these catalysts can potentially impact PEM fuel cell performance, where factors such as ionomer distribution, gaseous reactant transport, and water/thermal management become more important.

5.2   Recommendations for Future Work

A major limitation of this study is that the results are specific to Ketjen Black carbon. The effects of both oxidizing acid treatment and nitrogen doping on carbon microstructure and Pt NP morphology may differ for lower-area or more graphitized materials. Therefore, it would be worthwhile to try the alkaline EG+DMF catalyst synthesis method on different kinds of carbon to see if further improvements are possible. One idea is to combine functionalized KB with graphene to obtain a graphene / carbon black hybrid support [60]. This design would combine the unique benefits of functionalized KB (e.g., many nucleation sites for Pt) and graphene (e.g., high surface area and corrosion resistance), and the carbon black would prevent graphene layers from stacking, ensuring an adequately porous catalyst layer (CL). Single-cell testing would be needed to verify the effective transport of reactant gases, ions, and product water in the CL containing graphene and carbon black.

Another interesting topic touched upon in this thesis is the benefits of anisotropic Pt morphologies, such as nanowires and nanorods. The unexpected formation of nanorods in Pt/KB-10x suggests that these structures can be produced in a more controlled manner if the parameters of the alkaline EG+DMF method are optimized. A previous study used this method to obtain Pt nanowires supported on carbon nanotubes [52], but with much more solvent needed per unit mass of Pt compared to this work. It would be worthwhile to see if adjusting other parameters, such as temperature or basicity, could also increase nanowire yield. Moreover, little to no work has reported synthesis of 1- or 2-dimensional Pt structures in large quantities (e.g., gram scale). Developing a repeatable and scalable method for making carbon-supported Pt nanowires would be a major step forward in the practical application of these catalysts.

References

[1] International Energy Agency, "Global Energy Review 2021." https://www.iea.org/reports/global-energy-review-2021, 2021. Accessed: 2021-10-08.

[2] International Renewable Energy Agency, "Global energy transformation: A roadmap to 2050 (2019 edition)." https://www.irena.org/-/media/Files/IRENA/Agency/Publication/2019/Apr/IRENA_Global_Energy_Transformation_2019.pdf, 2019. Accessed: 2023-03-13.

[3] Natural Resources Canada, "Hydrogen Strategy for Canada (Seizing the Opportunities for Hydrogen)." https://natural-resources.canada.ca/sites/nrcan/files/environment/hydrogen/NRCan_Hydrogen-Strategy-Canada-na-en-v3.pdf, 2020. Accessed: 2023-03-13.

[4] X. Li, *Principles of Fuel Cells*. New York, NY: Taylor and Francis, 2006.

[5] A. Baroutaji, T. Wilberforce, M. Ramadan, and A. G. Olabi, "Comprehensive investigation on hydrogen and fuel cell technology in the aviation and aerospace sectors," *Renewable and Sustainable Energy Reviews*, vol. 106, pp. 31–40, 2019.

[6] D. Banham and S. Ye, "Current Status and Future Development of Catalyst Materials and Catalyst Layers for Proton Exchange Membrane Fuel Cells: An Industrial Perspective," *ACS Energy Letters*, vol. 2, pp. 629–638, 3 2017.

[7] D. Banham, J. Zou, S. Mukerjee, Z. Liu, D. Yang, Y. Zhang, Y. Peng, and A. Dong, "Ultralow platinum loading proton exchange membrane fuel cells: Performance losses and solutions," *Journal of Power Sources*, vol. 490, p. 229515, 2021.

[8] D. A. Cullen, K. C. Neyerlin, R. K. Ahluwalia, R. Mukundan, K. L. More, R. L. Borup, A. Z. Weber, D. J. Myers, and A. Kusoglu, "New roads and challenges for fuel cells in heavy-duty transportation," *Nature Energy*, vol. 6, no. 5, pp. 462–474, 2021.

[9] U.S. Department of Energy, "FY 2019 Progress Report for the DOE Hydrogen and Fuel Cells Program." https://www.hydrogen.energy.gov/pdfs/progress19/fc_overview_2019.pdf, 2020. Accessed: 2021-10-04.

[10] X. X. Wang, M. T. Swihart, and G. Wu, "Achievements, challenges and perspectives on cathode catalysts in proton exchange membrane fuel cells for transportation," *Nature Catalysis*, vol. 2, no. 7, pp. 578–589, 2019.

[11] A. Kongkanand and M. F. Mathias, "The Priority and Challenge of High-Power Performance of Low-Platinum Proton-Exchange Membrane Fuel Cells," *The Journal of Physical Chemistry Letters*, vol. 7, pp. 1127–1137, 4 2016.

[12] R. T. White, S. H. Eberhardt, Y. Singh, T. Haddow, M. Dutta, F. P. Orfino, and E. Kjeang, "Four-dimensional joint visualization of electrode degradation and liquid water distribution inside operating polymer electrolyte fuel cells," *Scientific Reports*, vol. 9, no. 1, p. 1843, 2019.

[13] B. Li, J. Wang, X. Gao, C. Qin, D. Yang, H. Lv, Q. Xiao, and C. Zhang, "High performance octahedral PtNi/C catalysts investigated from rotating disk electrode to membrane electrode assembly," *Nano Research*, vol. 12, no. 2, pp. 281–287, 2019.

[14] A. T. S. Freiberg, M. C. Tucker, and A. Z. Weber, "Polarization loss correction derived from hydrogen local-resistance measurement in low Pt-loaded polymer-electrolyte fuel cells," *Electrochemistry Communications*, vol. 79, pp. 14–17, 2017.

[15] H. Yu, L. Bonville, and R. Maric, "Analysis of H2/Air Polarization Curves: The Influence of Low Pt Loading and Fabrication Process," *Journal of The Electrochemical Society*, vol. 165, no. 5, pp. F272–F284, 2018.

[16] A. Mahata, A. S. Nair, and B. Pathak, "Recent advancements in Pt-nanostructure-based electrocatalysts for the oxygen reduction reaction," *Catalysis Science & Technology*, vol. 9, no. 18, pp. 4835–4863, 2019.

[17] J. K. Nørskov, J. Rossmeisl, A. Logadottir, L. Lindqvist, J. R. Kitchin, T. Bligaard, and H. Jónsson, "Origin of the Overpotential for Oxygen Reduction at a Fuel-Cell Cathode," *The Journal of Physical Chemistry B*, vol. 108, pp. 17886–17892, 11 2004.

[18] U.S. Department of Energy, "Multi-Year Research, Development, and Demonstration Plan: 3.4 Fuel Cells." https://www.energy.gov/sites/default/files/2017/05/f34/fcto_myrdd_fuel_cells.pdf, 2017. Accessed: 2021-10-04.

[19] Y.-J. Wang, W. Long, L. Wang, R. Yuan, A. Ignaszak, B. Fang, and D. P. Wilkinson, "Unlocking the door to highly active ORR catalysts for PEMFC applications: polyhedron-engineered Pt-based nanocrystals," *Energy & environmental science*, vol. 11, no. 2, pp. 258–275, 2018.

[20] G. J. Leong, M. C. Schulze, M. B. Strand, D. Maloney, S. L. Frisco, H. N. Dinh, B. Pivovar, and R. M. Richards, "Shape-directed platinum nanoparticle synthesis: nanoscale design of novel catalysts," *Applied Organometallic Chemistry*, vol. 28, pp. 1–17, 1 2014.

[21] T. Chu, M. Xie, D. Yang, P. Ming, B. Li, and C. Zhang, "Highly active and durable carbon support Pt-rare earth catalyst for proton exchange membrane fuel cell," *International Journal of Hydrogen Energy*, vol. 45, no. 51, pp. 27291–27298, 2020.

[22] K. Nagasawa, S. Takao, K. Higashi, S.-i. Nagamatsu, G. Samjeské, Y. Imaizumi, O. Sekizawa, T. Yamamoto, T. Uruga, and Y. Iwasawa, "Performance and durability of Pt/C cathode catalysts with different kinds of carbons for polymer electrolyte

fuel cells characterized by electrochemical and in situ XAFS techniques," *Physical Chemistry Chemical Physics*, vol. 16, no. 21, pp. 10075–10087, 2014.

[23] E. Padgett, V. Yarlagadda, M. E. Holtz, M. Ko, B. D. A. Levin, R. S. Kukreja, J. M. Ziegelbauer, R. N. Andrews, J. Ilavsky, A. Kongkanand, and D. A. Muller, "Mitigation of PEM Fuel Cell Catalyst Degradation with Porous Carbon Supports," *Journal of the Electrochemical Society*, vol. 166, no. 4, pp. F198–F207, 2019.

[24] P. Hernández-Fernández, M. Montiel, P. Ocón, J. L. G. de la Fuente, S. García-Rodríguez, S. Rojas, and J. L. G. Fierro, "Functionalization of multi-walled carbon nanotubes and application as supports for electrocatalysts in proton-exchange membrane fuel cell," *Applied Catalysis B: Environmental*, vol. 99, no. 1, pp. 343–352, 2010.

[25] S. Zhou, J. Zang, H. Gao, X. Tian, P. Tian, S. Song, and Y. Wang, "Deflagration method synthesizing N, S co-doped oxygen-functionalized carbons as a bifunctional catalyst for oxygen reduction and oxygen evolution reaction," *Carbon*, vol. 181, pp. 234–245, 2021.

[26] L. Pan, S. Ott, F. Dionigi, and P. Strasser, "Current challenges related to the deployment of shape-controlled Pt alloy oxygen reduction reaction nanocatalysts into low Pt-loaded cathode layers of proton exchange membrane fuel cells," *Current Opinion in Electrochemistry*, vol. 18, pp. 61–71, 2019.

[27] G. Niu, M. Zhou, X. Yang, J. Park, N. Lu, J. Wang, M. J. Kim, L. Wang, and Y. Xia, "Synthesis of PtNi Octahedra in Continuous-Flow Droplet Reactors for the Scalable Production of Highly Active Catalysts toward Oxygen Reduction," *Nano Letters*, vol. 16, pp. 3850–3857, 6 2016.

[28] H. Liu, J. Zhao, and X. Li, "Controlled Synthesis of Carbon-Supported Pt-Based Electrocatalysts for Proton Exchange Membrane Fuel Cells," *Electrochemical Energy Reviews*, vol. 5, no. 4, p. 13, 2022.

[29] S. Shahgaldi, J. Zhao, I. Alaefour, and X. Li, "Investigation of catalytic vs reactant transport effect of catalyst layers on proton exchange membrane fuel cell performance," *Fuel*, vol. 208, pp. 321–328, 2017.

[30] J. Fan, M. Chen, Z. Zhao, Z. Zhang, S. Ye, S. Xu, H. Wang, and H. Li, "Bridging the gap between highly active oxygen reduction reaction catalysts and effective catalyst layers for proton exchange membrane fuel cells," *Nature Energy*, vol. 6, no. 5, pp. 475–486, 2021.

[31] X. Cheng, G. Wei, C. Wang, S. Shen, and J. Zhang, "Experimental probing of effects of carbon support on bulk and local oxygen transport resistance in ultra-low Pt PEMFCs," *International Journal of Heat and Mass Transfer*, vol. 164, p. 120549, 2021.

[32] S. Ott, A. Orfanidi, H. Schmies, B. Anke, H. N. Nong, J. Hübner, U. Gernert, M. Gliech, M. Lerch, and P. Strasser, "Ionomer distribution control in porous carbon-supported catalyst layers for high-power and low Pt-loaded proton exchange membrane fuel cells," *Nature Materials*, vol. 19, no. 1, pp. 77–85, 2020.

[33] Y. Xia, X. Xia, and H.-C. Peng, "Shape-Controlled Synthesis of Colloidal Metal Nanocrystals: Thermodynamic versus Kinetic Products," *Journal of the American Chemical Society*, vol. 137, pp. 7947–7966, 7 2015.

[34] M. Schneider-Coppolino, S. Gautam, and B. D. Gates, "Chapter 17 - Nanocatalysts for proton exchange fuel cells: design, preparation, and utilization," in *PEM Fuel Cells* (G. Kaur, ed.), pp. 465–545, Elsevier, 2022.

[35] F. Li, X. Gao, Q. Xue, S. Li, Y. Chen, and J.-M. Lee, "Reduced graphene oxide supported platinum nanocubes composites: one-pot hydrothermal synthesis and enhanced catalytic activity," *Nanotechnology*, vol. 26, no. 6, p. 65603, 2015.

[36] R. Devivaraprasad, T. Kar, A. Chakraborty, R. K. Singh, and M. Neergat, "Reconstruction and dissolution of shape-controlled Pt nanoparticles in acidic electrolytes," *Physical Chemistry Chemical Physics*, vol. 18, no. 16, pp. 11220–11232, 2016.

[37] R. B. Moghaddam, S. Shahgaldi, and X. Li, "A facile synthesis of high activity cube-like Pt/carbon composites for fuel cell application," *Frontiers in Energy*, vol. 11, no. 3, pp. 245–253, 2017.

[38] P. Pei, M. Wang, D. Chen, P. Ren, and L. Zhang, "Key technologies for polymer electrolyte membrane fuel cell systems fueled impure hydrogen," *Progress in Natural Science: Materials International*, vol. 30, no. 6, pp. 751–763, 2020.

[39] R. M. Antoniassi, J. C. M. Silva, T. Lopes, A. Oliveira Neto, and E. V. Spinacé, "Carbon-supported Pt nanoparticles with (100) preferential orientation with enhanced electrocatalytic properties for carbon monoxide, methanol and ethanol oxidation in acidic medium," *International Journal of Hydrogen Energy*, vol. 42, no. 48, pp. 28786–28796, 2017.

[40] M. Rana, M. Chhetri, B. Loukya, P. K. Patil, R. Datta, and U. K. Gautam, "High-Yield Synthesis of Sub-10 nm Pt Nanotetrahedra with Bare 111 Facets for Efficient Electrocatalytic Applications," *ACS Applied Materials & Interfaces*, vol. 7, pp. 4998–5005, 3 2015.

[41] V. Tripković, I. Cerri, T. Bligaard, and J. Rossmeisl, "The Influence of Particle Shape and Size on the Activity of Platinum Nanoparticles for Oxygen Reduction Reaction: A Density Functional Theory Study," *Catalysis Letters*, vol. 144, no. 3, pp. 380–388, 2014.

[42] R. Subbaraman, D. Strmcnik, A. P. Paulikas, V. R. Stamenkovic, and N. M. Markovic, "Oxygen Reduction Reaction at Three-Phase Interfaces," *ChemPhysChem*, vol. 11, pp. 2825–2833, 9 2010.

[43] C. M. Sánchez-Sánchez, J. Solla-Gullón, F. J. Vidal-Iglesias, A. Aldaz, V. Montiel, and E. Herrero, "Imaging Structure Sensitive Catalysis on Different Shape-Controlled Platinum Nanoparticles," *Journal of the American Chemical Society*, vol. 132, pp. 5622–5624, 4 2010.

[44] K. Kodama, A. Shinohara, N. Hasegawa, K. Shinozaki, R. Jinnouchi, T. Suzuki, T. Hatanaka, and Y. Morimoto, "Catalyst Poisoning Property of Sulfonimide Acid

Ionomer on Pt (111) Surface," *Journal of The Electrochemical Society*, vol. 161, no. 5, pp. F649–F652, 2014.

[45] F. Zhou, Y. Yan, S. Guan, W. Guo, M. Sun, and M. Pan, "Solving Nafion poisoning of ORR catalysts with an accessible layer: designing a nanostructured core-shell Pt/C catalyst via a one-step self-assembly for PEMFC," *International Journal of Energy Research*, vol. 44, pp. 10155–10167, 10 2020.

[46] S. V. R., F. Ben, M. B. Simon, W. Guofeng, R. P. N., L. C. A., and M. N. M., "Improved Oxygen Reduction Activity on Pt3Ni(111) via Increased Surface Site Availability," *Science*, vol. 315, pp. 493–497, 1 2007.

[47] R. Sakamoto, K. Omichi, T. Furuta, and M. Ichikawa, "Effect of high oxygen reduction reaction activity of octahedral PtNi nanoparticle electrocatalysts on proton exchange membrane fuel cell performance," *Journal of Power Sources*, vol. 269, pp. 117–123, 2014.

[48] S. Y. Hwang, E. Yurchekfrodl, C. Zhang, and Z. Peng, "Low-Temperature Preferential Oxidation of Carbon Monoxide on Pt3Ni Alloy Nanoparticle Catalyst with Engineered Surface," *ChemCatChem*, vol. 8, pp. 97–101, 1 2016.

[49] R. Miao, F. Chang, M. Ren, X. He, L. Yang, X. Wang, and Z. Bai, "Platinum-palladium alloy nanotetrahedra with tuneable lattice-strain for enhanced intrinsic activity," *Catalysis Science & Technology*, vol. 10, no. 18, pp. 6173–6179, 2020.

[50] R. Wu, P. Tsiakaras, and P. K. Shen, "Facile synthesis of bimetallic Pt-Pd symmetry-broken concave nanocubes and their enhanced activity toward oxygen reduction reaction," *Applied Catalysis B: Environmental*, vol. 251, pp. 49–56, 2019.

[51] C. Chen, K. Yijin, H. Ziyang, Z. Zhongwei, H. Wenyu, X. H. L., S. J. D., L. Dongguo, H. J. A., M. Manos, C. Miaofang, M. K. L., L. Yadong, M. N. M., S. G. A., Y. Peidong, and S. V. R., "Highly Crystalline Multimetallic Nanoframes with Three-Dimensional Electrocatalytic Surfaces," *Science*, vol. 343, pp. 1339–1343, 3 2014.

[52] M. A. Hoque, F. M. Hassan, A. M. Jauhar, G. Jiang, M. Pritzker, J.-Y. Choi, S. Knights, S. Ye, and Z. Chen, "Web-like 3D Architecture of Pt Nanowires and Sulfur-Doped Carbon Nanotube with Superior Electrocatalytic Performance," *ACS Sustainable Chemistry & Engineering*, vol. 6, pp. 93–98, 1 2018.

[53] G. Prieto, J. Zecevic, H. Friedrich, K. P. De Jong, and P. E. De Jongh, "Towards stable catalysts by controlling collective properties of supported metal nanoparticles," *Nature Materials*, vol. 12, pp. 34–39, 1 2013.

[54] F. Rodríguez-reinoso, "The role of carbon materials in heterogeneous catalysis," *Carbon*, vol. 36, no. 3, pp. 159–175, 1998.

[55] H. Huang, H. Chen, D. Sun, and X. Wang, "Graphene nanoplate-Pt composite as a high performance electrocatalyst for direct methanol fuel cells," *Journal of Power Sources*, vol. 204, pp. 46–52, 2012.

[56] M. A. Molina-García and N. V. Rees, "Effect of catalyst carbon supports on the oxygen reduction reaction in alkaline media: a comparative study," *RSC Advances*, vol. 6, no. 97, pp. 94669–94681, 2016.

[57] S. M. Andersen, "Nano carbon supported platinum catalyst interaction behavior with perfluorosulfonic acid ionomer and their interface structures," *Applied Catalysis B: Environmental*, vol. 181, pp. 146–155, 2016.

[58] L. Işkel Şanl, V. Bayram, S. Ghobadi, N. Düzen, and S. Alkan Gürsel, "Engineered catalyst layer design with graphene-carbon black hybrid supports for enhanced platinum utilization in PEM fuel cell," *International Journal of Hydrogen Energy*, vol. 42, no. 2, pp. 1085–1092, 2017.

[59] A. Marinkas, F. Arena, J. Mitzel, G. M. Prinz, A. Heinzel, V. Peinecke, and H. Natter, "Graphene as catalyst support: The influences of carbon additives and catalyst preparation methods on the performance of PEM fuel cells," *Carbon*, vol. 58, pp. 139–150, 2013.

[60] Z. Ji, J. Chen, M. Pérez-Page, Z. Guo, Z. Zhao, R. Cai, M. T. P. Rigby, S. J. Haigh, and S. M. Holmes, "Doped graphene/carbon black hybrid catalyst giving enhanced oxygen reduction reaction activity with high resistance to corrosion in proton exchange membrane fuel cells," *Journal of Energy Chemistry*, vol. 68, pp. 143–153, 2022.

[61] Y. Luo, J. Feng, Y. Jiang, L. Li, and J. Feng, "Accessible mesoporous carbon aerogel preparation and its application as ultra-low pt support for oxygen reduction reaction with high catalytic activity," *Journal of Porous Materials*, vol. 28, no. 3, pp. 661–672, 2021.

[62] A. Guha, W. Lu, T. A. Zawodzinski, and D. A. Schiraldi, "Surface-modified carbons as platinum catalyst support for PEM fuel cells," *Carbon*, vol. 45, no. 7, pp. 1506–1517, 2007.

[63] V. Comignani, J. M. Sieben, M. D. Sanchez, and M. M. E. Duarte, "Influence of carbon support properties on the electrocatalytic activity of PtRuCu nanoparticles for methanol and ethanol oxidation," *International Journal of Hydrogen Energy*, vol. 42, no. 39, pp. 24785–24796, 2017.

[64] Y.-T. Kim and T. Mitani, "Competitive effect of carbon nanotubes oxidation on aqueous EDLC performance: Balancing hydrophilicity and conductivity," *Journal of Power Sources*, vol. 158, no. 2, pp. 1517–1522, 2006.

[65] S. Pérez-Rodríguez, E. Pastor, and M. J. Lázaro, "Electrochemical behavior of the carbon black Vulcan XC-72R: Influence of the surface chemistry," *International Journal of Hydrogen Energy*, vol. 43, no. 16, pp. 7911–7922, 2018.

[66] J. H. Kim, Y. Yuk, H. S. Joo, J. Y. Cheon, H. S. Choi, S. H. Joo, and J. Y. Park, "Nanoscale adhesion between Pt nanoparticles and carbon support and its influence on the durability of fuel cells," *Current Applied Physics*, vol. 15, pp. S108–S114, 2015.

[67] H. Schmies, E. Hornberger, B. Anke, T. Jurzinsky, H. N. Nong, F. Dionigi, S. Kühl, J. Drnec, M. Lerch, C. Cremers, and P. Strasser, "Impact of Carbon Support Func-

tionalization on the Electrochemical Stability of Pt Fuel Cell Catalysts," *Chemistry of Materials*, vol. 30, pp. 7287–7295, 10 2018.

[68] C. K. Acharya, W. Li, Z. Liu, G. Kwon, C. Heath Turner, A. M. Lane, D. Nikles, T. Klein, and M. Weaver, "Effect of boron doping in the carbon support on platinum nanoparticles and carbon corrosion," *Journal of Power Sources*, vol. 192, no. 2, pp. 324–329, 2009.

[69] V. Perazzolo, R. Brandiele, C. Durante, M. Zerbetto, V. Causin, G. A. Rizzi, I. Cerri, G. Granozzi, and A. Gennaro, "Density Functional Theory (DFT) and Experimental Evidences of MetalSupport Interaction in Platinum Nanoparticles Supported on Nitrogen- and Sulfur-Doped Mesoporous Carbons: Synthesis, Activity, and Stability," *ACS Catalysis*, vol. 8, pp. 1122–1137, 2 2018.

[70] X. Ning, Y. Li, B. Dong, H. Wang, H. Yu, F. Peng, and Y. Yang, "Electron transfer dependent catalysis of Pt on N-doped carbon nanotubes: Effects of synthesis method on metal-support interaction," *Journal of Catalysis*, vol. 348, pp. 100–109, 2017.

[71] Z. Fang, M. S. Lee, J. Y. Kim, J. H. Kim, and T. F. Fuller, "The Effect of Carbon Support Surface Functionalization on PEM Fuel Cell Performance, Durability, and Ionomer Coverage in the Catalyst Layer," *Journal of The Electrochemical Society*, vol. 167, no. 6, p. 064506, 2020.

[72] X. Wang, S. Yang, Y. Yu, M. Dou, Z. Zhang, and F. Wang, "Low-loading Pt nanoparticles embedded on Ni, N-doped carbon as superior electrocatalysts for oxygen reduction," *Catalysis Science & Technology*, vol. 10, no. 1, pp. 65–69, 2020.

[73] A. R. Corpuz, K. N. Wood, S. Pylypenko, A. A. Dameron, P. Joghee, T. S. Olson, G. Bender, H. N. Dinh, T. Gennett, R. M. Richards, and R. O'Hayre, "Effect of nitrogen post-doping on a commercial platinumruthenium/carbon anode catalyst," *Journal of Power Sources*, vol. 248, pp. 296–306, 2014.

[74] S.-I. Choi, S.-U. Lee, R. Choi, J. T. Park, and S. W. Han, "Nitrogen-Doped Pt/C Electrocatalysts with Enhanced Activity and Stability toward the Oxygen Reduction Reaction," *ChemPlusChem*, vol. 78, pp. 1252–1257, 10 2013.

[75] J. Quinson and K. M. . Jensen, "From platinum atoms in molecules to colloidal nanoparticles: A review on reduction, nucleation and growth mechanisms," *Advances in Colloid and Interface Science*, vol. 286, p. 102300, 2020.

[76] D. Dixon, J. Melke, M. Botros, J. Rathore, H. Ehrenberg, and C. Roth, "Increase of catalyst utilization in polymer electrolyte membrane fuel cells by shape-selected Pt nanoparticles," *International Journal of Hydrogen Energy*, vol. 38, no. 30, pp. 13393–13398, 2013.

[77] D. Li, C. Wang, D. S. Strmcnik, D. V. Tripkovic, X. Sun, Y. Kang, M. Chi, J. D. Snyder, D. van der Vliet, Y. Tsai, V. R. Stamenkovic, S. Sun, and N. M. Markovic, "Functional links between Pt single crystal morphology and nanoparticles with different size and shape: the oxygen reduction reaction case," *Energy & Environmental Science*, vol. 7, no. 12, pp. 4061–4069, 2014.

[78] J. Wang, B. Li, D. Yang, H. Lv, and C. Zhang, "Preparation of an octahedral PtNi/CNT catalyst and its application in high durability PEMFC cathodes," *RSC Advances*, vol. 8, no. 33, pp. 18381–18387, 2018.

[79] M. Shen, M. Xie, J. Slack, K. Waldrop, Z. Chen, Z. Lyu, S. Cao, M. Zhao, M. Chi, P. N. Pintauro, R. Cao, and Y. Xia, "PtCo truncated octahedral nanocrystals: a class of highly active and durable catalysts toward oxygen reduction," *Nanoscale*, vol. 12, no. 21, pp. 11718–11727, 2020.

[80] Y.-W. Lee, A.-R. Ko, S.-B. Han, H.-S. Kim, and K.-W. Park, "Synthesis of octahedral PtPd alloy nanoparticles for improved catalytic activity and stability in methanol electrooxidation," *Physical Chemistry Chemical Physics*, vol. 13, no. 13, pp. 5569–5572, 2011.

[81] H. J. Kim, B. Ruqia, M. S. Kang, S. B. Lim, R. Choi, K. M. Nam, W. S. Seo, G. Lee, and S.-I. Choi, "Shape-controlled Pt nanocubes directly grown on carbon supports and their electrocatalytic activity toward methanol oxidation," *Science Bulletin*, vol. 62, no. 13, pp. 943–949, 2017.

[82] Y. Liu, H. Chen, C. Tian, D. Geng, D. Wang, and S. Bai, "One-Pot Synthesis of Highly Efficient Carbon-Supported Polyhedral Pt3Ni Alloy Nanoparticles for Oxygen Reduction Reaction," *Electrocatalysis*, vol. 10, no. 6, pp. 613–620, 2019.

[83] L. Pak Hoe, M. Boaventura, T. Lagarteira, L. Kee Shyuan, and A. Mendes, "Polyol synthesis of reduced graphene oxide supported platinum electrocatalysts for fuel cells: Effect of Pt precursor, support oxidation level and pH," *International Journal of Hydrogen Energy*, vol. 43, no. 35, pp. 16998–17011, 2018.

[84] J. Quinson, M. Inaba, S. Neumann, A. A. Swane, J. Bucher, S. B. Simonsen, L. Theil Kuhn, J. J. K. Kirkensgaard, K. M. . Jensen, M. Oezaslan, S. Kunz, and M. Arenz, "Investigating Particle Size Effects in Catalysis by Applying a Size-Controlled and Surfactant-Free Synthesis of Colloidal Nanoparticles in Alkaline Ethylene Glycol: Case Study of the Oxygen Reduction Reaction on Pt," *ACS Catalysis*, vol. 8, pp. 6627–6635, 7 2018.

[85] M. K. Carpenter, T. E. Moylan, R. S. Kukreja, M. H. Atwan, and M. M. Tessema, "Solvothermal Synthesis of Platinum Alloy Nanoparticles for Oxygen Reduction Electrocatalysis," *Journal of the American Chemical Society*, vol. 134, pp. 8535–8542, 5 2012.

[86] C. Gumeci, A. Marathe, R. L. Behrens, J. Chaudhuri, and C. Korzeniewski, "Solvothermal Synthesis and Electrochemical Characterization of Shape-Controlled Pt Nanocrystals," *The Journal of Physical Chemistry C*, vol. 118, pp. 14433–14440, 7 2014.

[87] B. Y. Xia, H. B. Wu, Y. Yan, X. W. D. Lou, and X. Wang, "Ultrathin and Ultralong Single-Crystal Platinum Nanowire Assemblies with Highly Stable Electrocatalytic Activity," *Journal of the American Chemical Society*, vol. 135, pp. 9480–9485, 6 2013.

[88] X. Tan, S. Shahgaldi, and X. Li, "The effect of non-spherical platinum nanoparticle sizes on the performance and durability of proton exchange membrane fuel cells," *Advances in Applied Energy*, vol. 4, p. 100071, 2021.

[89] L. Zhang and Y. Xia, "Scaling up the Production of Colloidal Nanocrystals: Should We Increase or Decrease the Reaction Volume?," *Advanced Materials*, vol. 26, pp. 2600–2606, 4 2014.

[90] K.-C. Tsao and H. Yang, "Continuous Production of Carbon-Supported Cubic and Octahedral Platinum-Based Catalysts Using Conveyor Transport System," *Small*, vol. 12, pp. 4808–4814, 9 2016.

[91] Y. Tang, F. Gao, S. Yu, Z. Li, and Y. Zhao, "Surfactant-free synthesis of highly methanol-tolerant, polyhedral PdPt nanocrystallines for oxygen reduction reaction," *Journal of Power Sources*, vol. 239, pp. 374–381, 2013.

[92] B. Y. Xia, H. B. Wu, Y. Yan, H. B. Wang, and X. Wang, "One-Pot Synthesis of Platinum Nanocubes on Reduced Graphene Oxide with Enhanced Electrocatalytic Activity," *Small*, vol. 10, pp. 2336–2339, 6 2014.

[93] R. M. Antoniassi, H. Erikson, J. Solla-Gullón, R. M. Torresi, and J. M. Feliu, "Small (<5 nm), Clean, and Well-Structured Cubic Platinum Nanoparticles: Synthesis and Electrochemical Characterization," *ChemElectroChem*, vol. 8, pp. 49–52, 1 2021.

[94] S. Shahgaldi, I. Alaefour, and X. Li, "Impact of manufacturing processes on proton exchange membrane fuel cell performance," *Applied Energy*, vol. 225, pp. 1022–1032, 2018.

[95] M. Wang, J. H. Park, S. Kabir, K. C. Neyerlin, N. N. Kariuki, H. Lv, V. R. Stamenkovic, D. J. Myers, M. Ulsh, and S. A. Mauger, "Impact of Catalyst Ink Dispersing Methodology on Fuel Cell Performance Using in-Situ X-ray Scattering," *ACS Applied Energy Materials*, vol. 2, pp. 6417–6427, 9 2019.

[96] Y. Guo, F. Pan, W. Chen, Z. Ding, D. Yang, B. Li, P. Ming, and C. Zhang, "The Controllable Design of Catalyst Inks to Enhance PEMFC Performance: A Review," *Electrochemical Energy Reviews*, vol. 4, no. 1, pp. 67–100, 2021.

[97] S. Shukla, K. Domican, K. Karan, S. Bhattacharjee, and M. Secanell, "Analysis of Low Platinum Loading Thin Polymer Electrolyte Fuel Cell Electrodes Prepared by Inkjet Printing," *Electrochimica Acta*, vol. 156, pp. 289–300, 2015.

[98] K. Talukdar, S. Delgado, T. Lagarteira, P. Gazdzicki, and K. A. Friedrich, "Minimizing mass-transport loss in proton exchange membrane fuel cell by freeze-drying of cathode catalyst layers," *Journal of Power Sources*, vol. 427, pp. 309–317, 2019.

[99] N. Hasegawa, A. Kamiya, T. Matsunaga, N. Kitano, and M. Harada, "Analysis of crack formation during fuel cell catalyst ink drying process. Reduction of catalyst layer cracking by addition of high boiling point solvent," *Colloids and Surfaces A: Physicochemical and Engineering Aspects*, vol. 628, p. 127153, 2021.

[100] T. A. Greszler, D. Caulk, and P. Sinha, "The Impact of Platinum Loading on Oxygen Transport Resistance," *Journal of The Electrochemical Society*, vol. 159, no. 12, pp. F831–F840, 2012.

[101] S. Shahgaldi, A. Ozden, X. Li, and F. Hamdullahpur, "A scaled-up proton exchange membrane fuel cell with enhanced performance and durability," *Applied Energy*, vol. 268, p. 114956, 2020.

[102] J. Wang, B. Li, X. Gao, D. Yang, H. Lv, Q. Xiao, S. K. Kær, and C. Zhang, "From rotating disk electrode to single cell: Exploration of PtNi/C octahedral nanocrystal as practical proton exchange membrane fuel cell cathode catalyst," *Journal of Power Sources*, vol. 406, pp. 118–127, 2018.

[103] J. Wang, Q. Xue, B. Li, D. Yang, H. Lv, Q. Xiao, P. Ming, X. Wei, and C. Zhang, "Preparation of a Graphitized-Carbon-Supported PtNi Octahedral Catalyst and Application in a Proton-Exchange Membrane Fuel Cell," *ACS Applied Materials & Interfaces*, vol. 12, pp. 7047–7056, 2 2020.

[104] C. Kim and H. Lee, "Applying Shape-Controlled Pt Nano-dendrites Supported on Carbon for Membrane-Electrode Assembly in a Proton Exchange Membrane Fuel Cell," *Fuel Cells*, vol. 13, pp. 889–894, 10 2013.

[105] B. Fang, L. Daniel, A. Bonakdarpour, R. Govindarajan, J. Sharman, and D. P. Wilkinson, "Dense Pt Nanowire Electrocatalyst for Improved Fuel Cell Performance Using a Graphitic Carbon Nitride-Decorated Hierarchical Nanocarbon Support," *Small*, vol. 17, p. 2102288, 7 2021.

[106] J. Zhang, *PEM Fuel Cell Electrocatalysts and Catalyst Layers Fundamentals and Applications.* London: Springer, 2008.

[107] J. Wu, A. Gross, and H. Yang, "Shape and Composition-Controlled Platinum Alloy Nanocrystals Using Carbon Monoxide as Reducing Agent," *Nano Letters*, vol. 11, pp. 798–802, 2 2011.

[108] C.-Y. Ahn, J.-Y. Cheon, S.-H. Joo, and J. Kim, "Effects of ionomer content on Pt catalyst/ordered mesoporous carbon support in polymer electrolyte membrane fuel cells," *Journal of Power Sources*, vol. 222, pp. 477–482, 2013.

[109] F. Jiang, F. Zhu, F. Yang, X. Yan, A. Wu, L. Luo, X. Li, and J. Zhang, "Comparative Investigation on the Activity Degradation Mechanism of Pt/C and PtCo/C Electrocatalysts in PEMFCs during the Accelerate Degradation Process Characterized by an in Situ X-ray Absorption Fine Structure," *ACS Catalysis*, vol. 10, pp. 604–612, 1 2020.

[110] J. Chlistunoff and J.-M. Sansiñena, "On the use of Nafion(R) in electrochemical studies of carbon supported oxygen reduction catalysts in aqueous media," *Journal of Electroanalytical Chemistry*, vol. 780, pp. 134–146, 2016.

[111] T. Sutharssan, D. Montalvao, Y. K. Chen, W.-C. Wang, C. Pisac, and H. Elemara, "A review on prognostics and health monitoring of proton exchange membrane fuel cell," *Renewable and Sustainable Energy Reviews*, vol. 75, pp. 440–450, 2017.

[112] Y. Luo and K. Jiao, "Cold start of proton exchange membrane fuel cell," *Progress in Energy and Combustion Science*, vol. 64, pp. 29–61, 2018.

[113] D. N. Ozen, B. Timurkutluk, and K. Altinisik, "Effects of operation temperature and reactant gas humidity levels on performance of PEM fuel cells," *Renewable and Sustainable Energy Reviews*, vol. 59, pp. 1298–1306, 2016.

[114] M. B. Sassin, Y. Garsany, R. W. Atkinson, R. M. E. Hjelm, and K. E. Swider-Lyons, "Understanding the interplay between cathode catalyst layer porosity and thickness on transport limitations en route to high-performance PEMFCs," *International Journal of Hydrogen Energy*, vol. 44, no. 31, pp. 16944–16955, 2019.

[115] S. Ott, A. Bauer, F. Du, T. A. Dao, M. Klingenhof, A. Orfanidi, and P. Strasser, "Impact of Carbon Support Meso-Porosity on Mass Transport and Performance of PEMFC Cathode Catalyst Layers," *ChemCatChem*, vol. 13, pp. 4759–4769, 11 2021.

[116] T. Soboleva, X. Zhao, K. Malek, Z. Xie, T. Navessin, and S. Holdcroft, "On the Micro-, Meso-, and Macroporous Structures of Polymer Electrolyte Membrane Fuel Cell Catalyst Layers," *ACS Applied Materials & Interfaces*, vol. 2, pp. 375–384, 2 2010.

[117] M. Inagaki, M. Toyoda, Y. Soneda, and T. Morishita, "Nitrogen-doped carbon materials," *Carbon*, vol. 132, pp. 104–140, 2018.

[118] E. Hornberger, T. Merzdorf, H. Schmies, J. Hübner, M. Klingenhof, U. Gernert, M. Kroschel, B. Anke, M. Lerch, J. Schmidt, A. Thomas, R. Chattot, I. Martens, J. Drnec, and P. Strasser, "Impact of Carbon N-Doping and Pyridinic-N Content on the Fuel Cell Performance and Durability of Carbon-Supported Pt Nanoparticle Catalysts," *ACS Applied Materials & Interfaces*, vol. 14, pp. 18420–18430, 4 2022.

[119] K. Shinozaki, Y. Morimoto, B. S. Pivovar, and S. S. Kocha, "Suppression of oxygen reduction reaction activity on Pt-based electrocatalysts from ionomer incorporation," *Journal of Power Sources*, vol. 325, pp. 745–751, 2016.

[120] J. Speder, A. Zana, I. Spanos, J. J. K. Kirkensgaard, K. Mortensen, M. Hanzlik, and M. Arenz, "Comparative degradation study of carbon supported proton exchange membrane fuel cell electrocatalysts The influence of the platinum to carbon ratio on the degradation rate," *Journal of Power Sources*, vol. 261, pp. 14–22, 2014.

[121] M. F. Labata, G. Li, J. Ocon, and P.-Y. A. Chuang, "Insights on platinum-carbon catalyst degradation mechanism for oxygen reduction reaction in acidic and alkaline media," *Journal of Power Sources*, vol. 487, p. 229356, 2021.

[122] I. Pastoriza-Santos and L. M. Liz-Marzán, "Binary cooperative complementary nanoscale interfacial materials. Reduction of silver nanoparticles in DMF. Formation of monolayers and stable colloids," *Pure and Applied Chemistry*, vol. 72, no. 1-2, pp. 83–90, 2000.
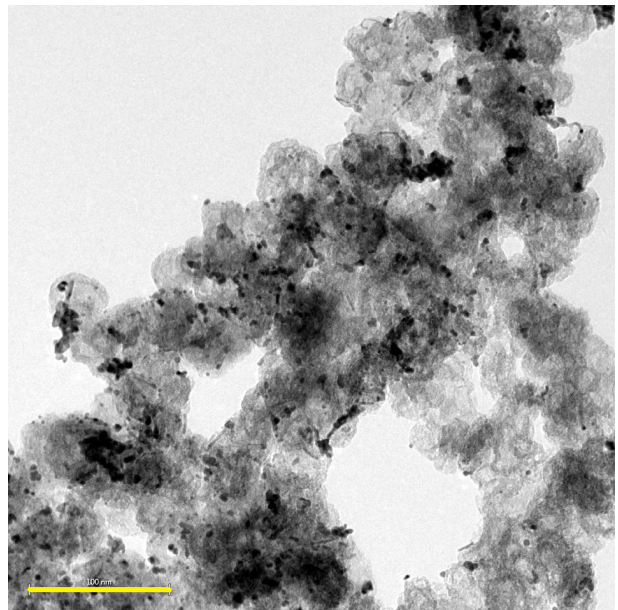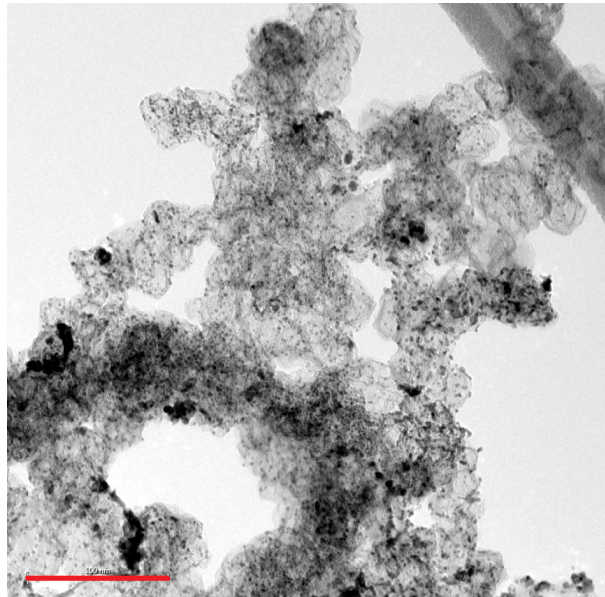
APPENDICES

Appendix A

Additional TEM Images
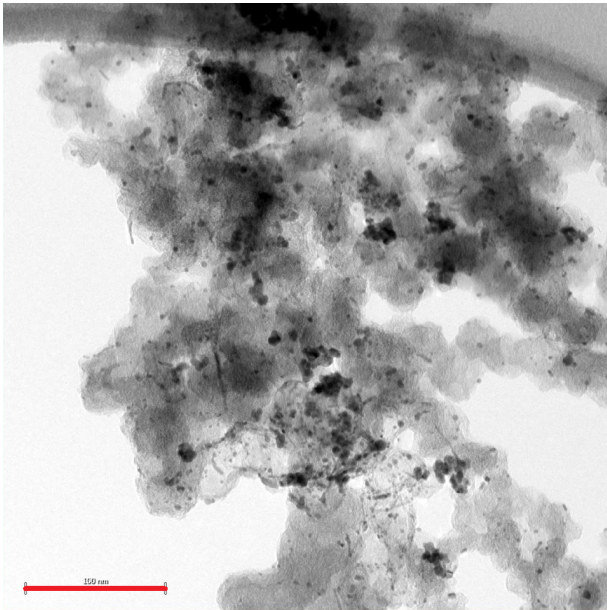
(a) Pt/KB-10x

(b) Pt/KB-O-10x

(c) Pt/KB-N-10x

Figure A.1: TEM images of the large-scale samples captured at 50kx magnification (scale bars are 100 nm)

(a) Pt/KB

(b) Pt/KB-10x

(c) Pt/KB-O

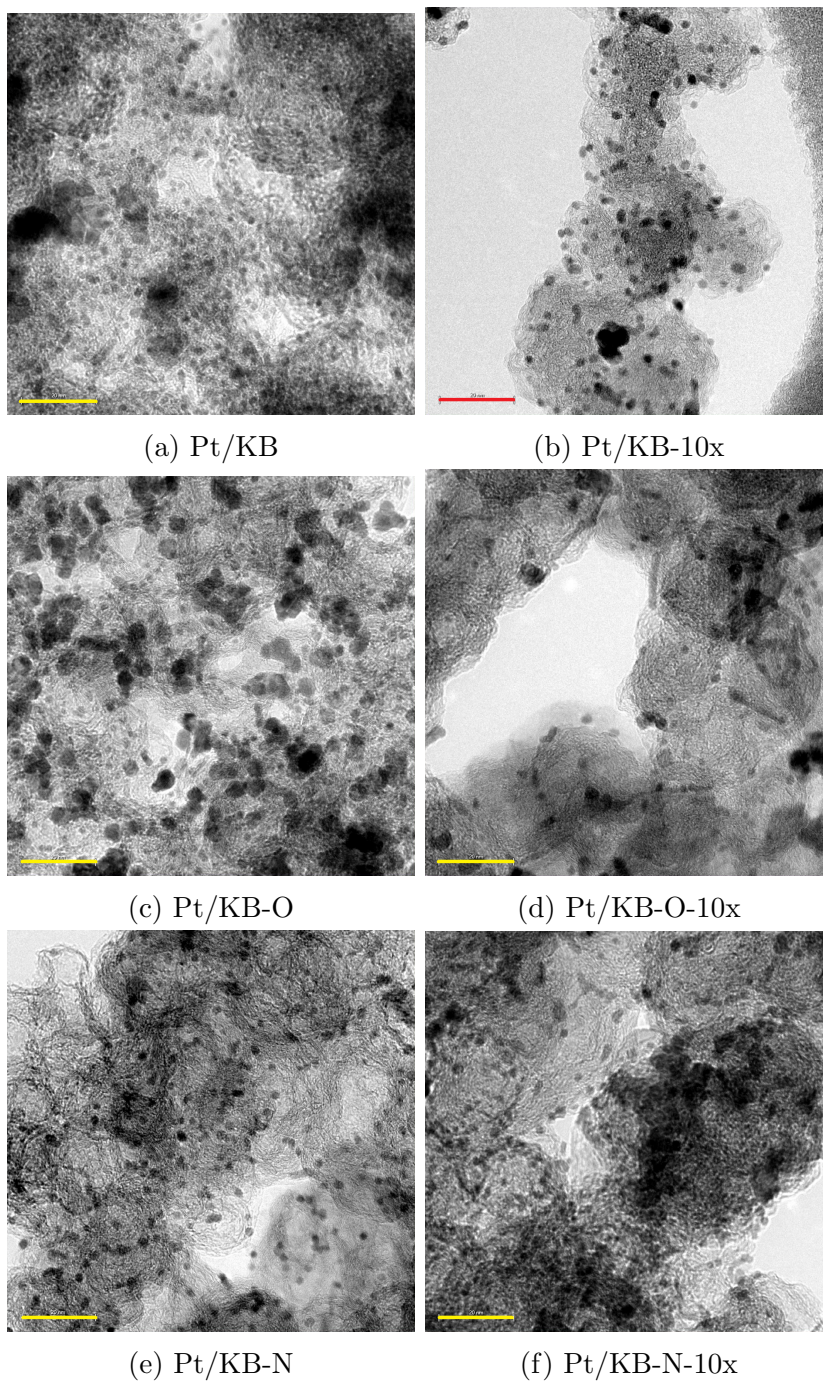(d) Pt/KB-O-10x

(e) Pt/KB-N

(f) Pt/KB-N-10x

Figure A.2: Additional TEM images captured at 200kx magnification (scale bars are 20 nm); most of these images are included in the particle size histograms.
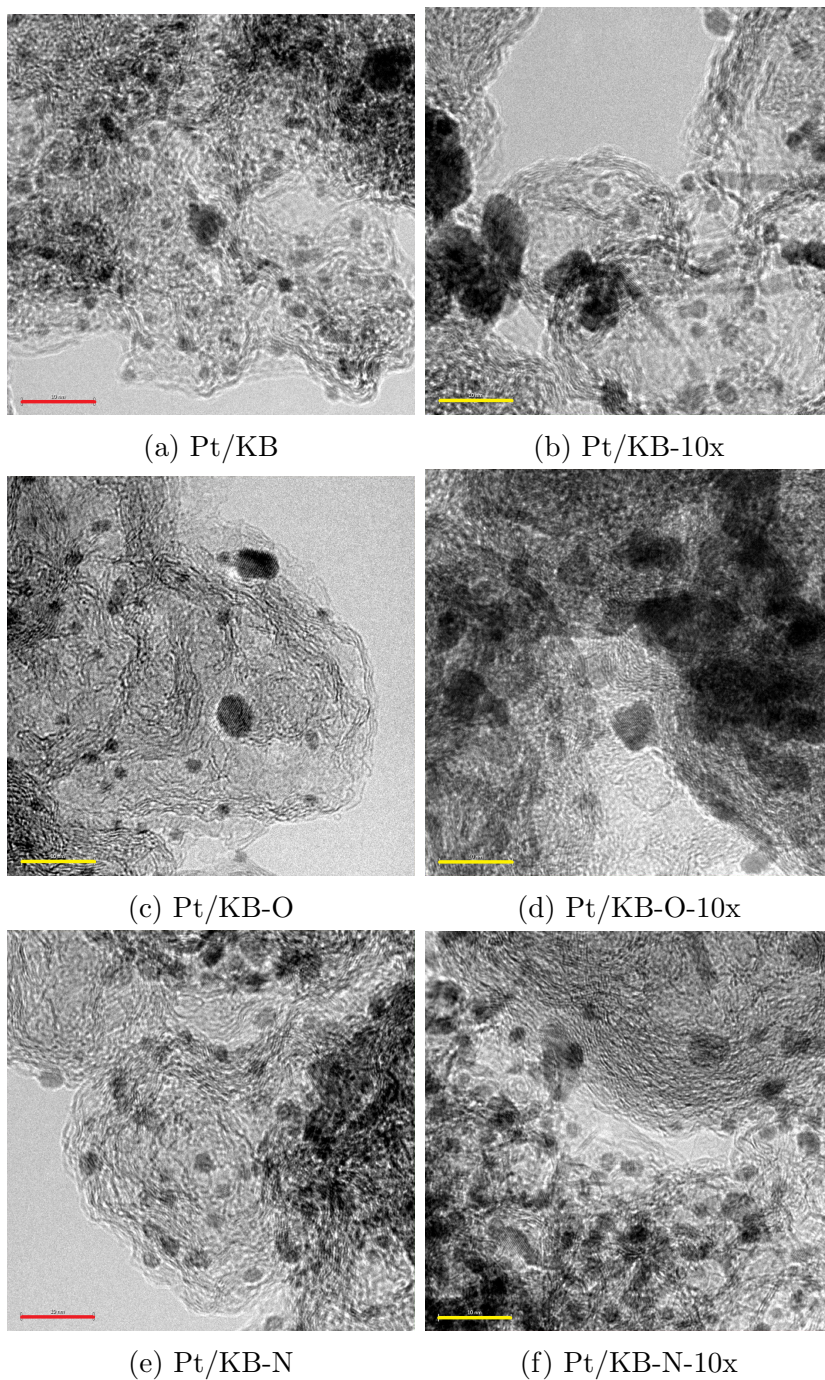
(a) Pt/KB   (b) Pt/KB-10x

(c) Pt/KB-O   (d) Pt/KB-O-10x

(e) Pt/KB-N   (f) Pt/KB-N-10x

Figure A.3: TEM images of all catalysts captured at 400kx magnification (scale bars are 10 nm)

(a) Pt/KB

(b) Pt/KB-10x

(c) Pt/KB-O

(d) Pt/KB-O-10x

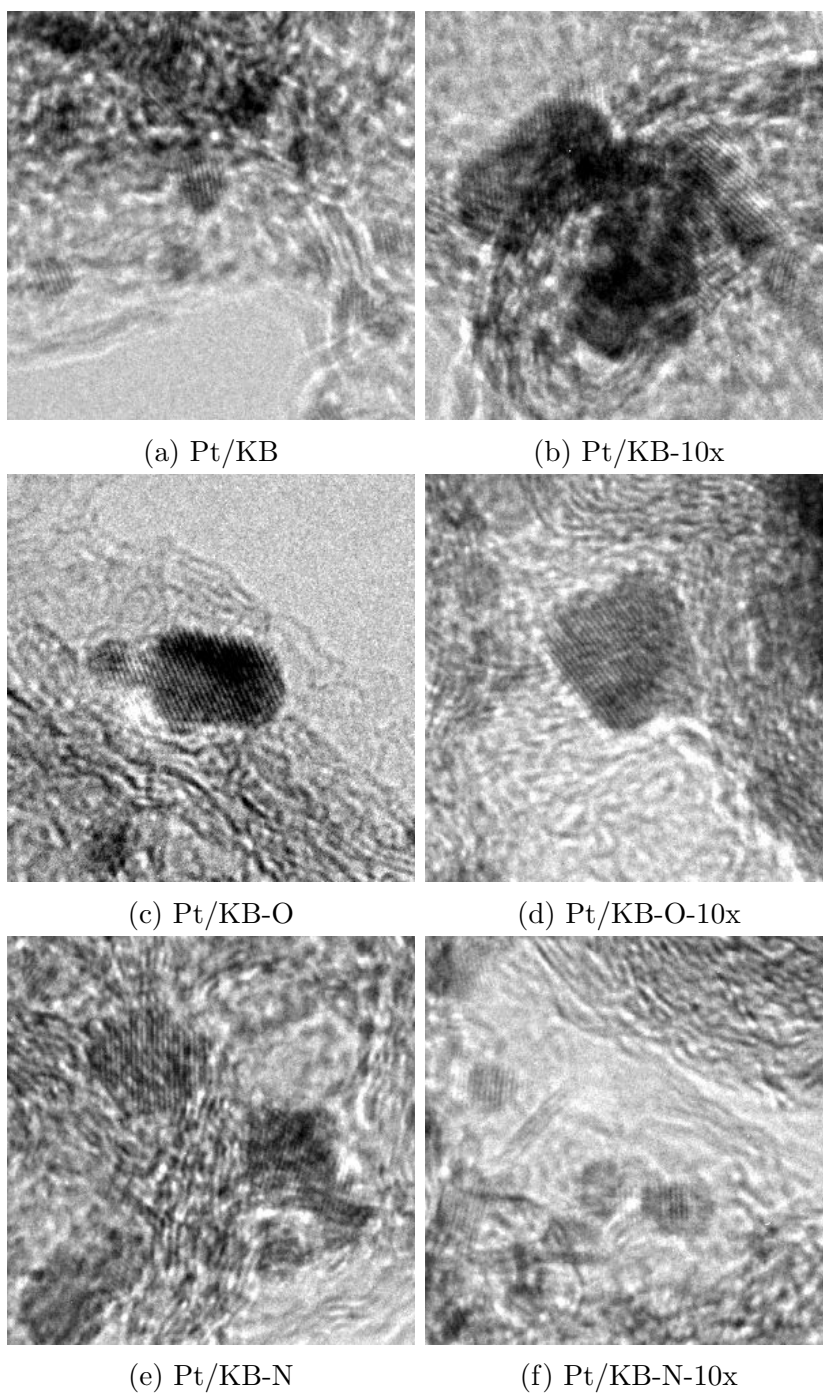(e) Pt/KB-N

(f) Pt/KB-N-10x

Figure A.4: Portions of TEM images of all catalysts captured at 400kx magnification

Appendix B

Additional Catalyst Synthesis Experiments

While developing the catalyst synthesis method for this thesis work, several samples were produced with slightly different synthesis procedures and parameters. This section presents physical characterization results for two of these samples.

Figure B.1 shows a TEM image and size histogram for a Pt/KB sample with 32 wt.% nominal Pt loading. This sample used 100 mg of carbon (instead of 40 mg) and 765 mg of NaOH (instead of 600 mg), and the Pt precursor and carbon were sonicated in separate solutions before combining for overnight stirring. Compared to the other catalysts presented in this thesis, the sample is dominated by medium-sized NPs (mean size of 4.6 nm) with high yield of polyhedral and cube-like shapes. A few smaller NPs and elongated shapes are also present. The NPs are dispersed evenly on the carbon support without much agglomeration. The TGA result for this sample estimates a Pt loading of 35.6 wt.%.
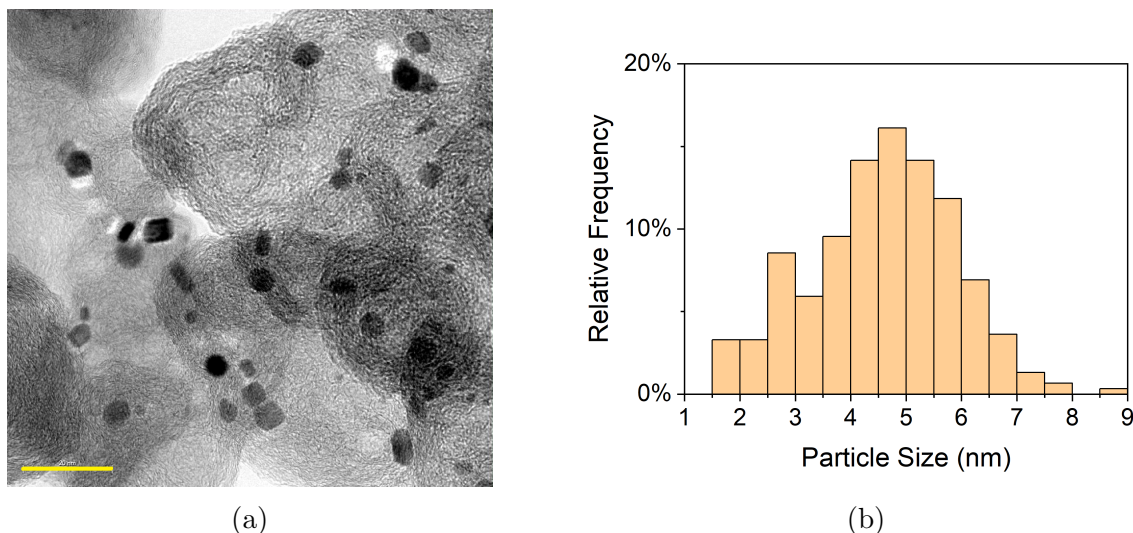
(a)   (b)

Figure B.1: a) TEM image captured at 200kx magnification (scale bar 20 nm); b) Size histogram based on two 100kx images

In another experiment, a Pt/KB sample (48.5 wt.% nominal Pt loading) was synthesized using 360 mg NaOH to determine if the original amount of 600 mg NaOH is truly necessary in the alkaline EG+DMF synthesis method. Like the Pt/KB sample shown in Chapter 4.2.1, this sample is dominated by small Pt NPs with mean size of 2.3 nm. However, TGA measurement records a Pt loading of only 40%. In addition, the solution in which the precursors reacted was observed to carry a slight orange/brown tint, similar to the color of the Pt precursor, suggesting that the precursor was not fully reduced. Therefore, a high concentration of NaOH is probably required to fulfill the reactions between the precursor, EG, DMF, and NaOH during the synthesis process. Various reaction mechanisms between metal precursors, DMF, and OH^- have been proposed in literature [86, 122]; these reactions generate secondary species (e.g., carbamic acid) that may help stabilize specific crystal facets, leading to shape-controlled growth of Pt NPs [86].